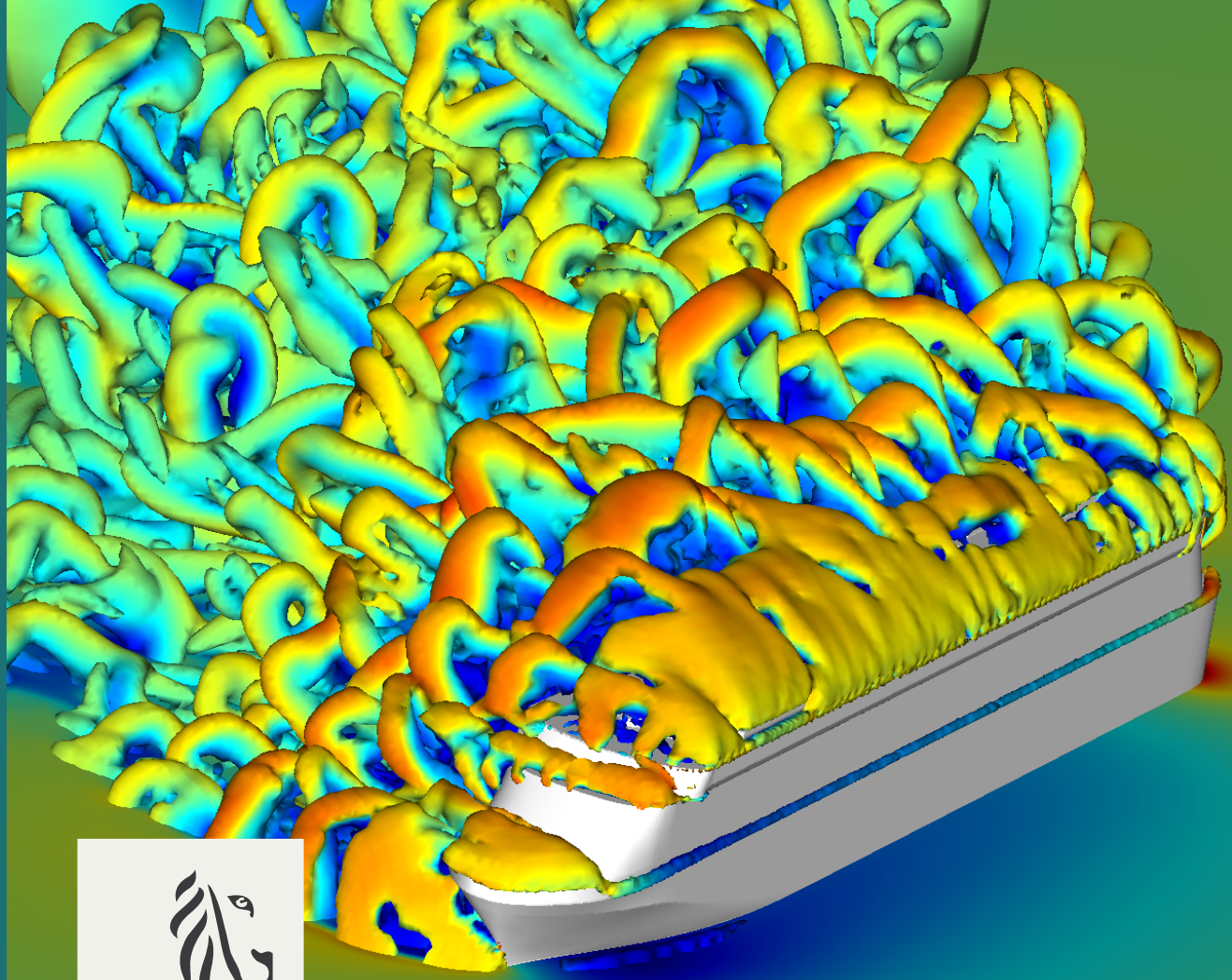

Flanders
State of
the Art

21_001_1
FHR reports

Modelling of ship behaviour in wind and current

Proof-of-concept of a method to account for arbitrary wind fields and wind field gradients in real-time simulations

DEPARTMENT
**MOBILITY &
PUBLIC
WORKS**

www.flandershydraulicsresearch.be

Modelling of ship behaviour in wind and current

Proof-of-concept of a method to account for arbitrary wind fields and wind field gradients in real-time simulations

Van Hoydonck, W.; Van Zwijnsvoorde, T.; Verwilligen, J.

Flanders Hydraulics Research
Flanders State of the Art

Cover figure © The Government of Flanders, Department of Mobility and Public Works, Flanders Hydraulics Research

Legal notice

Copyright and citation

D/2022/3241/191

This publication should be cited as follows:

Van Hoydonck, W.; Van Zwijnsvoorde, T.; Verwilligen, J. (2022). Modelling of ship behaviour in wind and current: Proof-of-concept of a method to account for arbitrary wind fields and wind field gradients in real-time simulations. Version 2.0. FHR Reports, 21_001_1. Flanders Hydraulics Research: Antwerp

Document identification

Customer:	Flanders Hydraulics Research	Ref.:	WL2022R21_001_1
Keywords (3-5):	CFD, wind coefficients, wind gradients, sheltering, atmospheric profile		
Knowledge domains:	Harbours and waterways > Manoeuvring behaviour > Wind > Numerical calculations		
Text (p.):	30	Appendices (p.):	9
Confidential:	No	☒ Available online	

Author(s):	Van Hoydonck, W.

Control

	Name	Signature
Revisor(s):	Van Zwijnsvoorde, T.	Getekend door:Thibaut Van Zwijnsvoorde Getekend op:2022-11-08 10:43:08 +01:0 Reden:Ik keur dit document goed Thibaut Van Zwijnsvoorde
Project leader:	Verwilligen, J.	Getekend door:Jeroen Verwilligen (Signat Getekend op:2022-11-07 13:50:06 +01:0 Reden:Ik keur dit document goed Jeroen Verwilligen

Approval

Head of division:	Bellafkih, A.	Getekend door:Abdelkarim Bellafkih (Sign Getekend op:2022-11-07 12:08:48 +01:0 Reden:Ik keur dit document goed Abdelkarim Bellafkih

Abstract

The objective of this report is to investigate a method to account for arbitrary wind fields and wind field gradients in the ship simulators at Flanders Hydraulics (FH). Instead of requiring specific sets of coefficients that each correspond to a certain wind velocity profile, a set of coefficients (determined in a uniform velocity field) is used that contains contributions of different parts of the hull: the ship is divided vertically in a number of layers and longitudinally in a number of sections. For each of these ship parts, the force and moment contributions at the global ship reference point are determined from the pressure distribution. To determine the total forces and moments acting on the hull during a simulation, a representative wind velocity and wind direction is required for each hull part. In the current investigation, vertical gradients in the wind field (as caused by the atmospheric boundary layer) and horizontal gradients in the wind field (due to sheltering behind objects) are treated separately. For these simplified conditions, the velocity field is sampled at one or multiple points per hull part either on a horizontal or vertical line and the reference velocity is obtained by taking the squared average. Repeating this for each hull part, all contributions can be added together to obtain the total wind forces and moments.

For a simplified cruise ship, partial wind coefficients are determined for different hull divisions. It is found that for three of the components (C_X, C_M and C_N), the contributions of the different hull parts counteract each other. For the other three force components (C_Y, C_Z and C_K), the contributions amplify each other. For example, all hull parts contain a lateral force component C_Y that points in the same direction, whereas for the yawing moment C_N (which itself is caused by the lateral force), the frontal and aft hull parts contribute opposing values to the total yawing moment.

The influence is determined on the forces and moments of the number of layers and sections in which the cruise ship hull is partitioned. Dividing the hull in three equally high layers is sufficient for simulating the effects of widely varying vertical gradients in the wind field. For horizontal gradients in the wind field, at least three sections are required to simulate with reasonable accuracy non-linearities caused by the counteracting force components C_X, C_M and C_N. Five sections are likely sufficient for use in a real-time simulation environment.

It is concluded that, qualitatively speaking, the method works as expected for the cases that were investigated. With this method, both horizontal and vertical gradients in the wind field can be combined without requiring modifications on the ship side. It is recommended to implement a method like this in the simulator at FH in the near future. Future research could amongst others focus on how the global wind field in the simulator can be altered locally to account for the presence of large objects close to the simulation vessel.

Contents

List of Figures

List of Tables

Nomenclature

Abbreviations

CAD	Computer Aided Design
CFD	Computational Fluid Dynamics
FH	Flanders Hydraulics
JIP	Joint Industry Project
LNG	Liquefied Natural Gas

Latin symbols

A_F	Frontal projected area	m^2
A_L	Lateral projected area	m^2
B	ship beam	m
C_K	Non-dimensional moment around the x-axis	$-$
C_M	Non-dimensional moment around the y-axis	$-$
C_N	Non-dimensional moment around the z-axis	$-$
C_X	Non-dimensional force in the x-direction	$-$
C_Y	Non-dimensional force in the y-direction	$-$
C_Z	Non-dimensional force in the z-direction	$-$
H_{max}	Maximum height of the vessel	m
L_{oa}	Length over all	m
L_{pp}	Length between perpendiculars	m
n_l	Number of layers	$-$
N_s	Number of refinements on the body	$-$
n_s	Number of sections	$-$
N_w	Number of refinements in the wake	$-$
q	Dynamic pressure	Pa
V_s	Ship velocity	m/s
V_w	Wind velocity	m/s
$V_{w,max}$	Maximum wind velocity	m/s
$V_{w,min}$	Minimum wind velocity	m/s
V_∞	Reference velocity	m/s
z	Vertical coordinate and height above the water level	m
z_0	Roughness height	m
z_{ref}	Reference height	m/s

Greek symbols

φ	Angle of relative wind, $0°$ is head wind, increasing counterclockwise as seen from above	$°$

1 Introduction

1.1 Background

Recently, a study has been finalised to evaluate the Gerris Flow Solver[1] for the computation of wind coefficients (Van Hoydonck *et al.*, 2022). It was concluded that despite some limitations, Gerris can be used to compute ship wind coefficients subject to a uniform flow field. It was also stated that more work is required to implement more realistic conditions in the simulator to account for the effects of an atmospheric boundary layer (vertical gradient in the wind field) and partial sheltering behind other objects (horizontal gradient in the wind field).

In the current report, research is documented where a method is investigated to account for wind field gradients in real-time simulations in a uniform way. The reader can find more background information related to the computation of wind coefficients for ships in Van Hoydonck *et al.* (2022) and the references therein.

1.2 Methodology

The ship hull in Gerris is divided both longitudinally and vertically in multiple complementary parts (see Fig. 1 for an example with three longitudinal sections and two vertical layers). By computing the forces and moments on the parts separately, a set of partial wind coefficients is obtained in addition to a single set of coefficients for the whole hull. Using these partial wind coefficient sets in a simulation, the forces and moments on each hull part are computed separately using a local velocity value. The total force and moment components are then obtained by adding the partial force and moment components together.

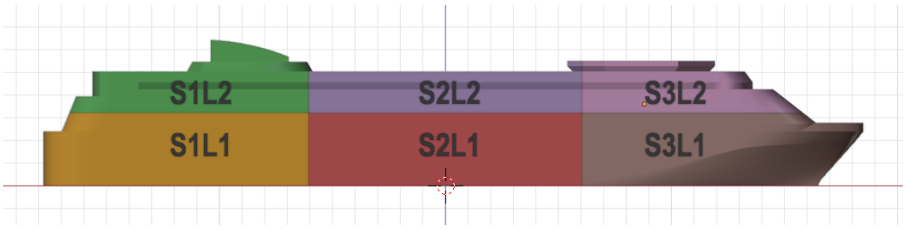

Figure 1 – Sideview of the hull of the WINDLASS cruise ship (Pietersma and Schrijvers, 2021) divided in three sections and two layers.

In principle, this method can account for the influence of gradients in the longitudinal and vertical direction on the resulting forces and moments on a ship hull. To account for lateral gradients in the wind field (e.g. in a head-on wind condition where a ship is sailing behind another ship that partially blocks the wind field), a further lateral division (port and starboard) of the hull could be implemented. At the moment, this is not pursued because the focus of the current research is on showing that the concept works. However, the author does not foresee any inherent limitation that would prevent one from adding a lateral division as well (other than that the Gerris Computational Fluid Dynamics (CFD) computations should be adapted and rerun). Another limitation of the current methodology is that the wind coefficients are computed assuming a uniform velocity field while these coefficient sets are used to simulate gradients in the wind field, (in part) caused by viscosity. For example, the horseshoe vortex that wraps around the base of wall-mounted cubes in viscous flows[2] at

[1] `https://gfs.sourceforge.net`

[2] See Hosker Jr. (1984) for more information on the physical phenomena occurring near wall-mounted objects in flows with or without gradients.

its influence on the resultant forces is not present here. These effects are considered as higher-order and neglected.

1.3 Ship geometry

The ship geometry used for the current research is the geometry of a simplified cruise ship[3], as used in the Windlass[4] JIP, see Fig. 2. For that project, Marin computed using their in-house CFD code ReFRESCO the wind coefficients of five ships for use in the Windlass software tool (Pietersma and Schrijvers, 2021). One of the differences with the current approach is that Marin computed the coefficients for a specific velocity profile (the Frøya profile that is representative for an open ocean (Andersen and Løvseth, 2006; Det Norske Veritas, 2014)) with a reference velocity of $25\,\mathrm{m/s}$ at the reference altitude of $10\,\mathrm{m}$, while here, a uniform wind field is assumed. Relevant characteristics of the cruise ship geometry for wind computations are gathered in Table 1.

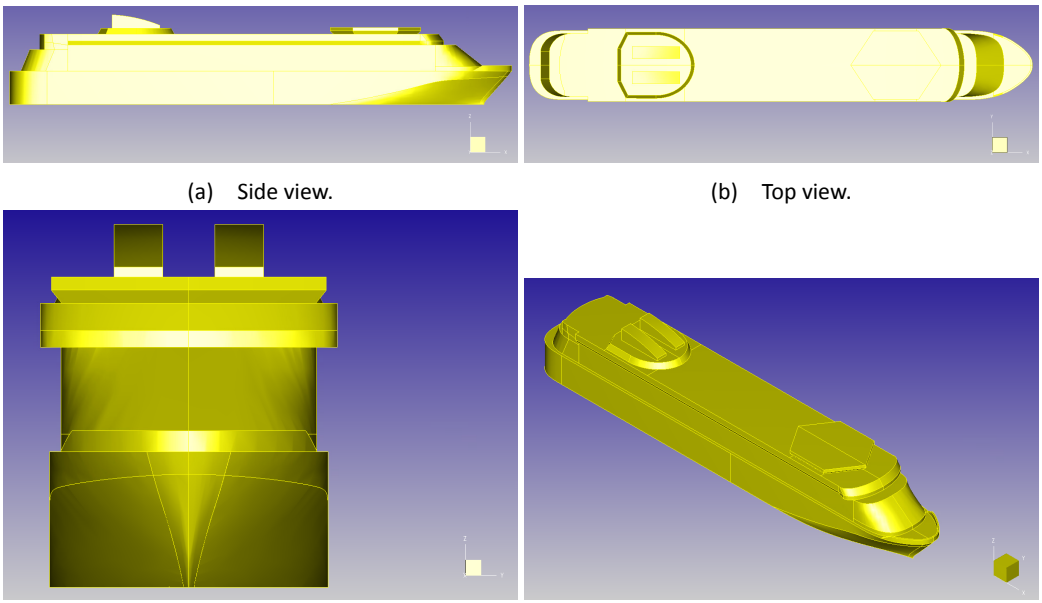

(a) Side view. (b) Top view.

(c) Front view. (d) Isometric view.

Figure 2 – Hull shape of the reference ship as used in JIP WINDLASS (Pietersma and Schrijvers, 2021).

Table 1 – Particulars of the Windlass cruise ship (Pietersma and Schrijvers, 2021).

Symbol	Value
L_{pp}	$330.0\,\mathrm{m}$
L_{oa}	$363.0\,\mathrm{m}$
B	$50.0\,\mathrm{m}$
H_{max}	$60.0\,\mathrm{m}$
A_F	$2818.1\,\mathrm{m}^2$
A_L	$17\,532.3\,\mathrm{m}^2$

[3] Note that the hull part below the waterline is not included in the Computer Aided Design (CAD) model: a draft value is not defined for this hull geometry.

[4] See `https://www.marin.nl/en/jips/windlass` for more details.

1.4 Alternative ship geometries

The sensitivity of the ship geometry on the coefficients is investigated by executing additional computations using two alternative stern geometries. The alternatives are shown in Fig. 3 together with the original rounded stern geometry. These alternatives do not alter the frontal and lateral silhouettes of the vessel, but may still have a significant impact on the aerodynamic forces and moments since flow will separate at the sharp edges (which affects the pressure distribution). whereas for the original smooth stern geometry, flow will remain attached for a longer period.

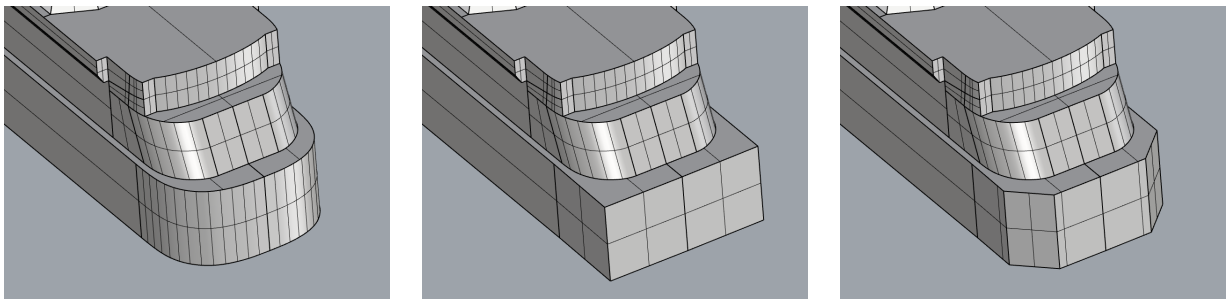

(a) Original stern. (b) Straight stern. (c) Chamfered stern.

Figure 3 – Original and two alternative stern geometries for the Windlass cruise ship.

1.5 Simulation conditions

1.5.1 Horizontal wind field gradients

To explore the influence of horizontal gradients in the wind field, the ship is assumed to sail along the X-axis (from positive to negative x) while the wind blows in the direction of positive y (see Fig. 4). For the current investigation, the contribution of the ship's speed is neglected when determining the angle of the relative wind, so in this case, it is exactly $\varphi = 90°$. In reality, the wind angle φ would be smaller than $90°$: for a ship speed $V_s = 2.5\,\mathrm{m/s}$ and a wind speed of $V_w = 25\,\mathrm{m/s}$ perpendicular to the heading of the vessel, $\varphi \approx 84°$.

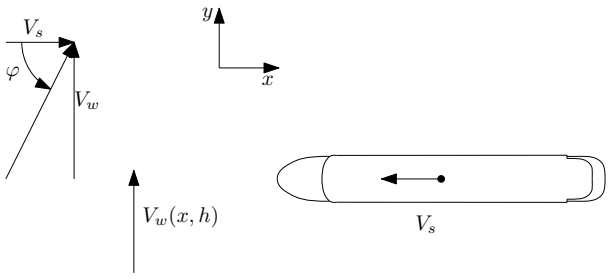

Figure 4 – Schematic view of the ship sailing in a wind field.

The velocity field is halved from its initial value of $V_{w,max} = 25\,\mathrm{m/s}$ when the x-coordinate changes sign. Halving the velocity magnitude will reduce the forces and moments by a factor four. Two wind profiles are tested, a scaled Heaviside (step) function and the following sigmoid function,

$$V_w(x) = \frac{1}{1 + \exp(-x)}(V_{w,max} - V_{w,min}) + V_{w,min}. \tag{1}$$

In addition to these two deterministic profiles, a third wind profile is considered by adding a quasi-random signal to the sigmoid function. All three profiles are shown in Fig. 5.

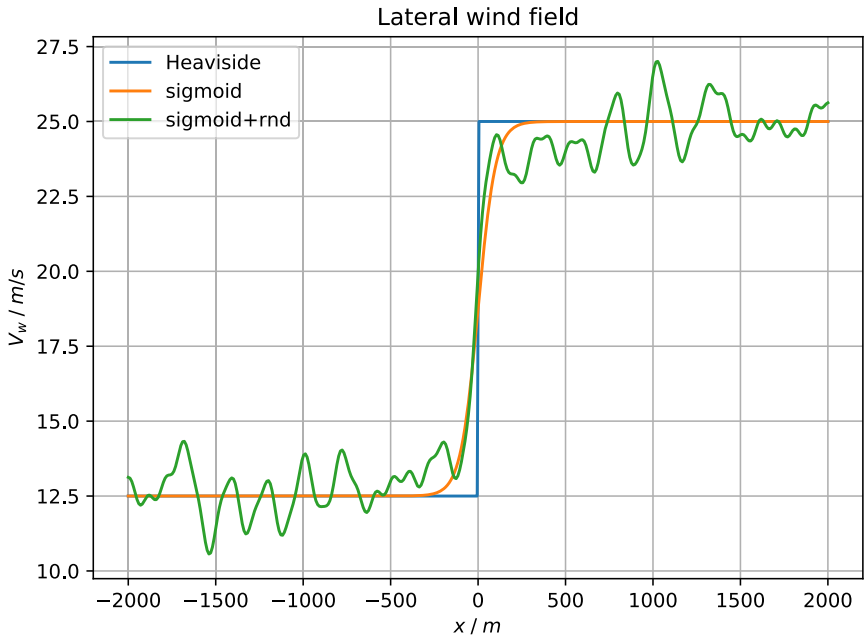

Figure 5 – Lateral wind speed V_w profiles as a function of longitudinal position x.

1.5.2 Vertical wind field gradients

The influence of vertical gradients on the forces and moments exerted on the ship hull are determined using the aforementioned *Frøya* wind profile (with the dependency of the profile on time removed),

$$V(z) = V_\infty \left(1 + 0.0573\sqrt{1 + 0.148V_\infty} \log \frac{z}{z_{ref}}\right), \tag{2}$$

and a generic logarithmic profile with a high roughness to mimic a profile in a port environment,

$$V(z) = V_\infty \frac{\log \frac{z+z_0}{z_0}}{\log \frac{z_{ref}+z_0}{z_0}} \tag{3}$$

where $z_0 = 0.4\,\text{m}$ is the roughness height.

For the reference condition as used by Marin ($V_{ref} = 25\,\text{m/s}$ at $z_{ref} = 10\,\text{m}$), both atmospheric velocity profiles are shown in Fig. 6 together with the associated distribution of the dynamic pressure $q(z)$.

Note that whenever vertical velocity profiles are utilised that require a reference velocity V_∞ at a reference height z_{ref}, the relative height of the ship with respect to the reference height is a key factor for the magnitude of the forces. If the vessel is significantly taller than the reference height (as is the case for the cruise ship), the use of an atmospheric profile will result in forces that are higher than when a uniform velocity field is used. If the vessel height is smaller or of the same order as the reference height, the resultant forces will be smaller than the forces due to a uniform velocity field. As an example, when the reference height is set to $z_{ref} = 60\,\text{m}$ (which equals the height of the cruise ship), the resulting Frøya and logarithmic profiles are shown in Fig. 7. The difference between both profiles is now significantly lower than when $z_{ref} = 10\,\text{m}$ (Fig. 6). This means that for a vessel with a low superstructure height (such an inland vessel), the actual atmospheric velocity profile does not matter as much as it does for a tall ship. This will be verified as well using the cruise ship by subjecting it to the velocity profiles shown in Fig. 7 (with the reference height set to $60\,\text{m}$).

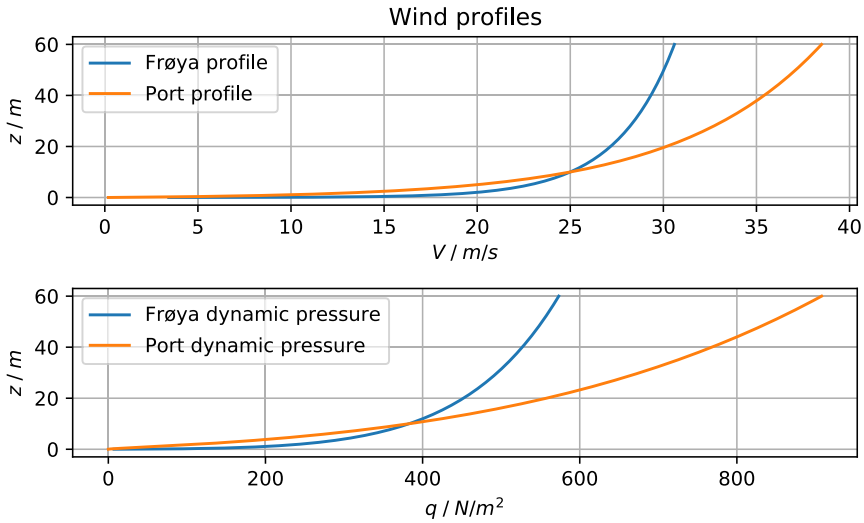

Figure 6 – Atmospheric velocity profiles (top) and associated dynamic pressure (bottom) profiles.

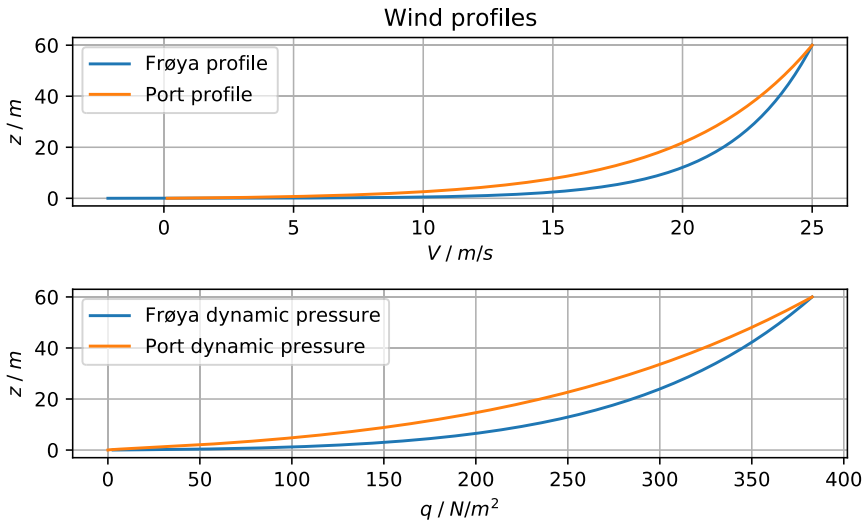

Figure 7 – Atmospheric velocity profiles (top) and associated dynamic pressure (bottom) profiles with $z_{ref} = 60$ m.

1.6 Report contents

The report is structured as follows:

- the partitioning strategy and the CFD setup is discussed;
- results of CFD computations with various hull divisions are presented and discussed, including a check on the convergence of the results as a function of the maximum refinement level;
- partial coefficients are used to simulate the effect of both horizontal and vertical gradients in the wind field;
- the report ends with conclusions and recommendations.

2 Hull partitioning and CFD setup

2.1 Hull partitioning

2.1.1 Introduction

Partitioning determines the boundaries of the hull parts for which forces and moments are separately computed. All partial forces and moments are determined at the same reference point, which means that they can be added together if needed (coefficients for the full hull are found by adding all partial coefficients together).

In Windlass (Pietersma and Schrijvers, 2021), hulls are partitioned in four parts. The hull is vertically divided at the location of the deck, and the top part (superstructure) is furthermore divided in three longitudinal sections (front, mid and aft). The bottom half of the hull is not split in the longitudinal direction. The relative sizes of the three longitudinal sections are specifically chosen to fit the geometry of the vessel: for the cruise ship, their length is approximately the same, but for other ships (such as the prismatic Liquefied Natural Gas (LNG)), there is a significant difference in the length of the parts.

For the current investigation, a simple scheme is used that can be easily adapted and automated because it is not known beforehand how many sections and layers are required to account for gradients in the wind field. Between the minimum[5] ($z = 0$ m) and maximum[6] (z = H_{max}) vertical extents of the hull geometry, the hull is split in n_l equally high layers: $\Delta z = \frac{H_{max}}{n_l}$. In the longitudinal direction between the aftmost and foremost points on the ship, the hull is split in n_s equally long sections, with each section having a length of $\Delta x = \frac{L_{oa}}{n_s}$. Layers are numbered starting from the bottom, and sections are numbered starting from the stern. An example with two layers and three sections was shown in Fig. 1. Table 2 shows the different partitionings of the cruise ship hull geometry (including the case without divisions: one layer and one section) that will be tested and compared in the current research. Visualisations of the hull divisions for cases 2S2L, 4S3L and 5S3L are displayed in Appendix A1 (Figs. 28, 30 and 32).

Table 2 – Hull partitionings of the cruise ship.

case	n_s	n_l
1S1L	1	1
2S2L	2	2
3S2L	3	2
4S3L	4	3
5S3L	5	3

2.1.2 Gerris

2.1.2.1 Axes systems

The wind axes system used in the current research follows the convention as used by Blendermann and Andersen (Andersen, 2007; Andersen, 2013; Blendermann, 2013), where the relative wind angle is measured

[5] $z = 0$ m corresponds to the waterline.
[6] H_{max} corresponds to the airdraft of the ship.

starting at the bow and increasing in counter clockwise direction (see Fig. 8). Coefficients are resolved at the intersection of the hull with the waterline in the lateral symmetry plane at the midship location. The default ship-fixed axes system is used. As a consequence, the drag (C_X) due to wind is negative for $\varphi = 0°$ and the lateral force is positive for $0° < \varphi < 180°$ and negative between $180°$ and $360°$.

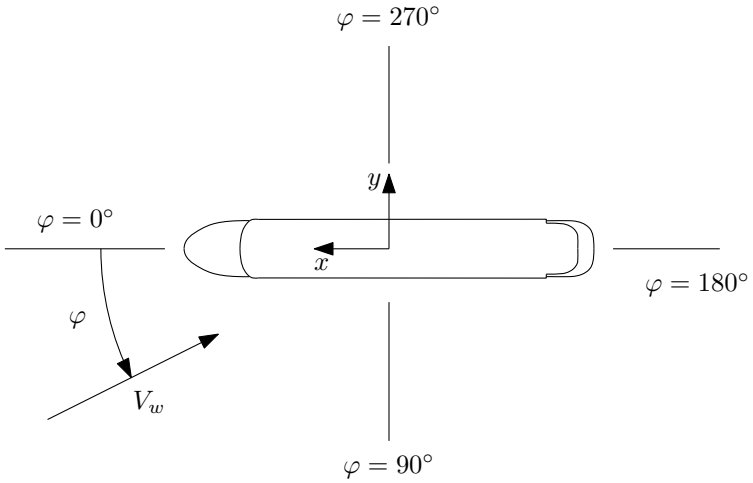

Figure 8 – Definition of the wind angle φ and the ship-fixed axes system in which the wind coefficients are defined.

2.1.2.2 Split forces output

The configuration script for a Gerris computation must contain the boundaries of the different parts such that the solver can compute partial forces and moments. A Python script has been developed to generate these parts in a semi-automatic way[7]. The input for this script are the extents of the ship hull when aligned with the X-axis of the global axis system: the locations of the extrema of the hull in longitudinal direction (stern and bow) and the extrema of the hull in vertical direction. Using these limiting values and the number of sections and layers, the script determines the bounds of the different parts and generates expressions to instruct the solver to restrict the force computation to certain parts of the domain.

Consider point $\bar{p}_1 = (x_1, y_1) = (r\cos\alpha, r\sin\alpha)$ in Fig. 9. In order to compare its location with respect to the x-bounds, the point is rotated over φ,

$$\bar{p}_r = (x_r, y_r) = (r\cos(\alpha + \varphi), r\sin(\alpha + \varphi)), \tag{4}$$

which can be written as

$$\begin{aligned} \bar{p}_r = (x_r, y_r) &= (r\cos(\alpha + \varphi), r\sin(\alpha + \varphi)) &(5)\\ &= (r\cos\alpha\cos\varphi - r\sin\alpha\sin\varphi, r\sin\alpha\cos\varphi + r\cos\alpha\sin\varphi). &(6)\end{aligned}$$

Substituting the Cartesian coordinates of point $\bar{p}_1$ into Eq. 5 results in

$$\begin{aligned} x_r &= x_1\cos\theta - y_1\sin\theta &(7)\\ y_r &= x_1\sin\theta + y_1\cos\theta). &(8)\end{aligned}$$

For comparison of the x-bounds, only the equation for x_r is required:

$$x_{min} < x\cos\varphi - y\sin\varphi <= x_{max} \tag{9}$$

[7]This script is part of the *cfd_utils* repository of repoSPNumMod and can be found at `https://wl-subversion.vlaanderen.be/svn/repoSpNumMod/Python/cfd_utils/trunk/cfd/gerris_hull_cut_planes.py`

while for the comparison of the z-bounds (when using multiple layers), the following comparison is used:

$$z_{min} < z <= z_{max}, \tag{10}$$

where x, y and z are the coordinates of a point in the global axes system of Gerris.

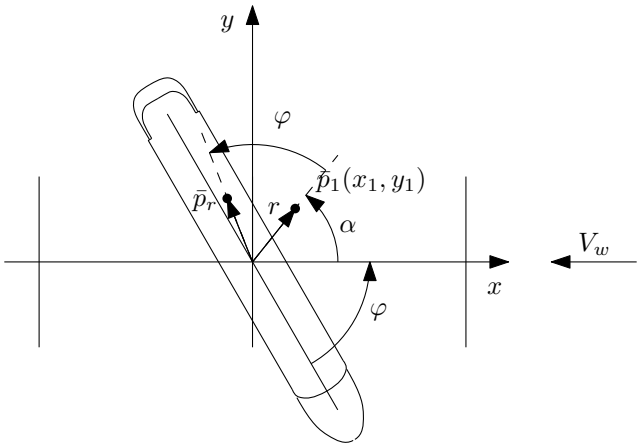

Figure 9 – Rotation of point $\bar{p}_1$ in the global axis system to align with x-bounds in the ship axis system.

For the case with two layers and three sections ($n_l = 2$ and $n_s = 3$), the output of this script for the cruise ship (scaled down to a length of 1/6 of the domain box to ensure that blockage is negligible) is shown in Listing 1. The code lines that starts with *Define*, are placed before the line that contains the term *GfsSimulation*. The lines starting with *OutputSolidForce* must be copied inside the body of the *GfsSimulation* command.

For each partial force computation, the resultant forces and moments are written to a separate file. The filenames of these files are also defined with the aforementioned Python script. Some of the configuration options (such as the maximum refinement on the hull and in the wake, and the angle of the hull with respect to the oncoming flow) are part of the names of the output files to make them unique, because multiple (slightly different) Gerris computations can be run from the same directory, generating output in the same folder.

Listing 1 – Gerris code to compute split forces ($n_s = 3$ and $n_l = 2$) on the ship hull.

```
Define XSECT3_0 -0.08336851
Define XSECT3_1 -0.02614637
Define XSECT3_2 0.02940911
Define XSECT3_3 0.08663126
Define ZSECT2_0 -0.50029515
Define ZSECT2_1 -0.48524241
Define ZSECT2_2 -0.47018967
Define FORCES forces-ANGLE-MAXREF-WAKEMAXREF.dat
Define FORCES6_S1_L1 forces6_S1_L1-ANGLE-MAXREF-WAKEMAXREF.dat
Define FORCES6_S1_L2 forces6_S1_L2-ANGLE-MAXREF-WAKEMAXREF.dat
Define FORCES6_S2_L1 forces6_S2_L1-ANGLE-MAXREF-WAKEMAXREF.dat
Define FORCES6_S2_L2 forces6_S2_L2-ANGLE-MAXREF-WAKEMAXREF.dat
Define FORCES6_S3_L1 forces6_S3_L1-ANGLE-MAXREF-WAKEMAXREF.dat
Define FORCES6_S3_L2 forces6_S3_L2-ANGLE-MAXREF-WAKEMAXREF.dat
  OutputSolidForce { istep = 1 } FORCES
  OutputSolidForce { istep = 1 } FORCES6_S1_L1 ( XSECT3_0 < x*cos( ANGLE_RAD ) - y*sin( ANGLE_RAD ) \
    && x*cos( ANGLE_RAD ) - y*sin( ANGLE_RAD ) <= XSECT3_1 && ZSECT2_0 < z && z <= ZSECT2_1)
  OutputSolidForce { istep = 1 } FORCES6_S1_L2 ( XSECT3_0 < x*cos( ANGLE_RAD ) - y*sin( ANGLE_RAD ) \
    && x*cos( ANGLE_RAD ) - y*sin( ANGLE_RAD ) <= XSECT3_1 && ZSECT2_1 < z && z <= ZSECT2_2)
  OutputSolidForce { istep = 1 } FORCES6_S2_L1 ( XSECT3_1 < x*cos( ANGLE_RAD ) - y*sin( ANGLE_RAD ) \
    && x*cos( ANGLE_RAD ) - y*sin( ANGLE_RAD ) <= XSECT3_2 && ZSECT2_0 < z && z <= ZSECT2_1)
  OutputSolidForce { istep = 1 } FORCES6_S2_L2 ( XSECT3_1 < x*cos( ANGLE_RAD ) - y*sin( ANGLE_RAD ) \
    && x*cos( ANGLE_RAD ) - y*sin( ANGLE_RAD ) <= XSECT3_2 && ZSECT2_1 < z && z <= ZSECT2_2)
  OutputSolidForce { istep = 1 } FORCES6_S3_L1 ( XSECT3_2 < x*cos( ANGLE_RAD ) - y*sin( ANGLE_RAD ) \
    && x*cos( ANGLE_RAD ) - y*sin( ANGLE_RAD ) <= XSECT3_3 && ZSECT2_0 < z && z <= ZSECT2_1)
  OutputSolidForce { istep = 1 } FORCES6_S3_L2 ( XSECT3_2 < x*cos( ANGLE_RAD ) - y*sin( ANGLE_RAD ) \
    && x*cos( ANGLE_RAD ) - y*sin( ANGLE_RAD ) <= XSECT3_3 && ZSECT2_1 < z && z <= ZSECT2_2)
```

2.1.2.3 Parameter variations

Apart from the number of sections and layers in which the force computation is divided, three parameters are altered for the current investigation: the maximum refinement level on the ship, the maximum refinement level in the wake and the increment $\Delta\varphi$ between different wind angles. At Marin, wind coefficient computations are executed with an increment of $\Delta\varphi = 15°$, while at FH, the increment is normally $\Delta\varphi = 10°$. For a range of $180°$, using the larger increment of $\Delta\varphi = 15°$ reduces the number of computations from 19 to 13. This obviously has an influence on the required computational resources, but it may also affect the resulting coefficient curves: at locations with significant gradients in the trends, extrema may be underpredicted.

Coarse, *medium* and *fine* computations will be executed at all wind angles from $0°$ to $180°$ with increments of $\Delta\varphi = 10°$ and $\Delta\varphi = 15°$. The differences in the settings between the *coarse*, *medium* and *fine* computations are related to the maximum refinement level on the hull and in its wake (see Table 3). As was already observed in Van Hoydonck *et al.* (2022), the maximum refinement level has a significant impact on the computing time while at the same time, the simulation time to arrive at a steady solution depends on the wind angle: simulation times are longer for angles near $\varphi = 90°$, than for angles near $\varphi = 0°$ and $\varphi = 180°$. A formal grid convergence analysis will not be undertaken, for the current research, it is deemed sufficient that there is overall convergence as the maximum refinement level is increased. The cell count for the three refinement settings (*coarse*, *medium* and *fine*) for $\varphi = 90°$ at the end of the simulation are 73×10^3, 380×10^3 and 2.342×10^6.

Table 3 – Refinement settings for the hull and wake for the grid convergence study.

	N_s	N_w
coarse	10	8
medium	11	9
fine	12	10

2.1.2.4 Scaling

In Gerris, a computational domain is created from one or multiple cubes with an unit edge length. In the previous report (Van Hoydonck *et al.*, 2022), it was found that in order to have negligible blockage inside the domain, the ship should occupy no more than $\frac{1}{6}$ of the edge length of the default domain cube. At this small size, the domain can be composed of a single box. The overall length of the ship is $363\,\text{m}$ (see Table 1), from which follows that the reference scale is $\frac{1}{6*363} = \frac{1}{2178} = 4.5913 \times 10^{-4}$. When the same reference speed as employed by Marin ($V_\infty = 25\,\text{m/s}$) is used to scale velocity, the scaling factor for the velocity components is 25. Time is scaled as well, one dimensionless second in Gerris corresponds to $\frac{Lref}{Vref} = \frac{2178}{25} = 87.12\,\text{s}$ in real life. By default, the computations will be run for two seconds, but this value may be increased if time histories of force components show that more time is required to reach a steady state. For the hull refinement levels as shown in Table 3, the smallest details that can be resolved are $2.13\,\text{m}$ ($N_s = 10$), $1.06\,\text{m}$ ($N_s = 11$) and $0.53\,\text{m}$ ($N_s = 12$).

2.1.3 Marin CFD results

Marin has computed wind coefficients for the cruise ship as part of the Windlass JIP(Pietersma and Schrijvers, 2021). These coefficients are determined with the Frøya atmospheric profile with $V_\infty = 25\,\text{m/s}$ at the standard altitude of $10\,\text{m}$. For the current research, wind coefficients for the cruise ship are computed assuming a uniform velocity field. The vertical division of the partial wind coefficients obtained as such will be used to approximate the coefficients obtained by Marin by using suitable velocities for each layer. Marin uses a different local coordinate system to define wind coefficients: the resultant wind angle is $0°$ with wind coming from the

stern, $90°$ with wind coming from starboard and $180°$ when the wind comes from the bow. The values from Marin are reproduced from tabular values in Pietersma and Schrijvers (2021), extended to the full $360°$ and converted to the axes system used here (Fig. 10).

Marin uses the following equations to make the forces and moments non-dimensional,

$$C_i = \frac{F_i}{1/2\rho U_{ref}^2 A_{F,i}}, \tag{11}$$

$$Cn_i = \frac{M_i}{1/2\rho U_{ref}^2 A_{M,i}}, \tag{12}$$

with i the three directions X, Y and Z. The reference areas $A_{F,i}$ and $A_{M,i}$ are listed in Table 4, reproduced from Pietersma and Schrijvers (2021, Table 1).

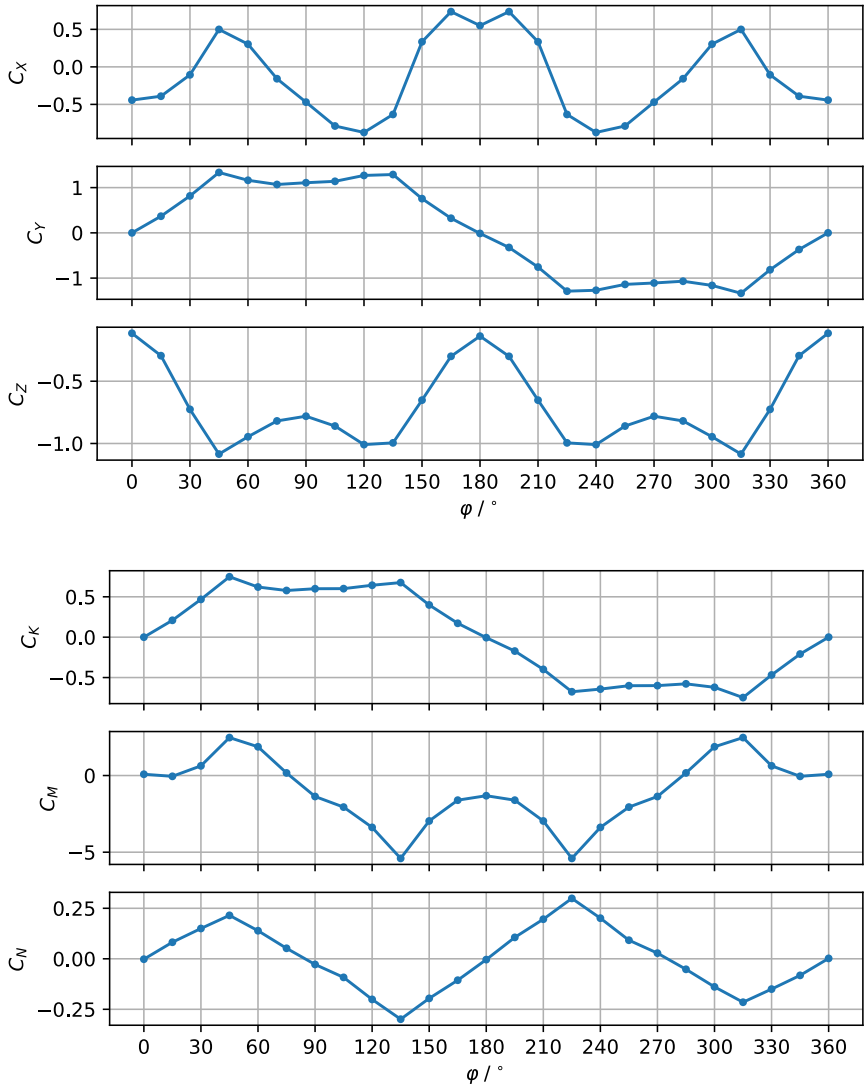

Figure 10 – Wind coefficients of the cruise ship as used in the WINDLASS JIP (Pietersma and Schrijvers, 2021).

Table 4 – Main particulars cruise ship (Pietersma and Schrijvers, 2021).

Designation	Symbol	Value
Length between perpendiculars	L_{pp}	$330\,\text{m}$
Breadth	B	$50\,\text{m}$
Maximum height from still water line	H_{max}	$60\,\text{m}$
Reference area Cx	A_F	$2818.1\,\text{m}$
Reference area Cy	A_L	$17\,532.3\,\text{m}$
Reference area Cz	$L_{pp} \cdot B$	$16\,500.0\,\text{m}$
Reference area Cnx	${A_L}^2/L_{pp}$	$9\,314\,569.2\,\text{m}$
Reference area Cny	${A_F}^2/B$	$158\,833.8\,\text{m}$
Reference area Cnz	$L_{pp} \cdot A_L$	$5\,785\,659.0\,\text{m}$
Reference velocity	V_∞	$5\,785\,659.0\,\text{m}$

3 CFD results

3.1 Time histories

Plotting the time histories of the forces and moments on the ship hull of the individual computations have revealed that for wind angles in the range $50° <= \varphi <= 120°$, convergence is not sufficient after two (dimensionless) seconds. For these cases, the end time is increased to four seconds. As an example, for $\varphi = 0°$ and $\varphi = 60°$ for computations with the medium refinement settings (N_s = 11 and N_w = 9), the time histories of four force coefficients are shown in Fig. 11.

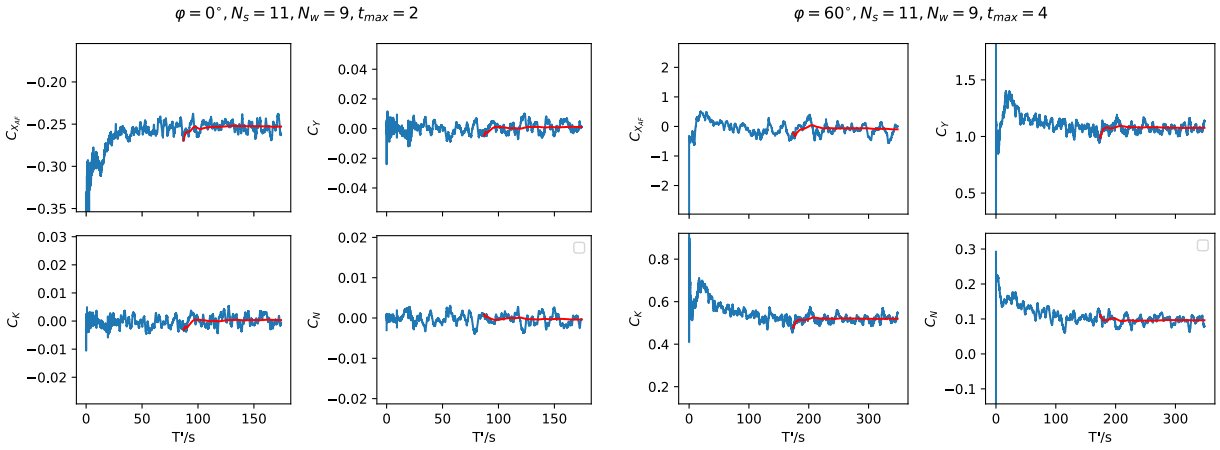

(a) $\varphi = 0°$ (b) $\varphi = 60°$

Figure 11 – Convergence of force coefficients for two wind angles for the medium refinement settings.

3.2 Maximum refinement level

First, the influence of the maximum refinement level on the resulting forces and moments will be determined. As stated before, three sets of computations[8] are performed with increasing maximum refinement for both the ship and the wake of the ship with wind angles from $0°$ to $180°$. Results are shown for a wind angle increment $\Delta\varphi = 15°$ in Fig. 12 for all force components and for each component, the numerical result of Marin is included as a reference. Note however that the purpose is not to obtain a perfect (or even good) match with the results of Marin since the boundary conditions are not the same (a uniform wind field for the results of Gerris and an atmospheric boundary layer for the results of Marin).

The differences between the coarse and medium results are larger than the differences between the medium and fine results. This is especially true for the lateral force C_Y, the roll moment C_K and the yawing moment C_N. For the longitudinal force C_X at $\varphi = 90°$ and the vertical force C_Z at $\varphi = 45°$, the medium result is closer to the coarse result than it is to the fine result. However, for the rest of the angles, the results do show converging trends.

Overall, the current results show similar trends as the results of Marin, although extrema do not necessarily

[8] Note that the graphs in this chapter show results for the full $360°$, while computations have only been performed for angels in the range $0°$ to $180°$.

have the same value. This is however expected, because the integral of the dynamic pressure over the height of the ship results in a larger value for the atmospheric profile than the the equivalent dynamic pressure integral using a uniform velocity field. Also, Marin included the viscous contribution in the coefficients. For some combinations of wind angles and force components (e.g. C_X near $0°$ and $180°$ and C_Z near $90°$), the viscous contribution add somewhat to the total force. For the wind-facing side of the hull near $\varphi = 90°$, the resultant viscous force will be directed upward, which may increase the total vertical force on the hull in addition to the contribution due to pressure. This viscous force component also contributes to the roll moment C_K, which may explain to some extent the discrepancy between the prediction of Marin and the current values near $\varphi = 90°$.

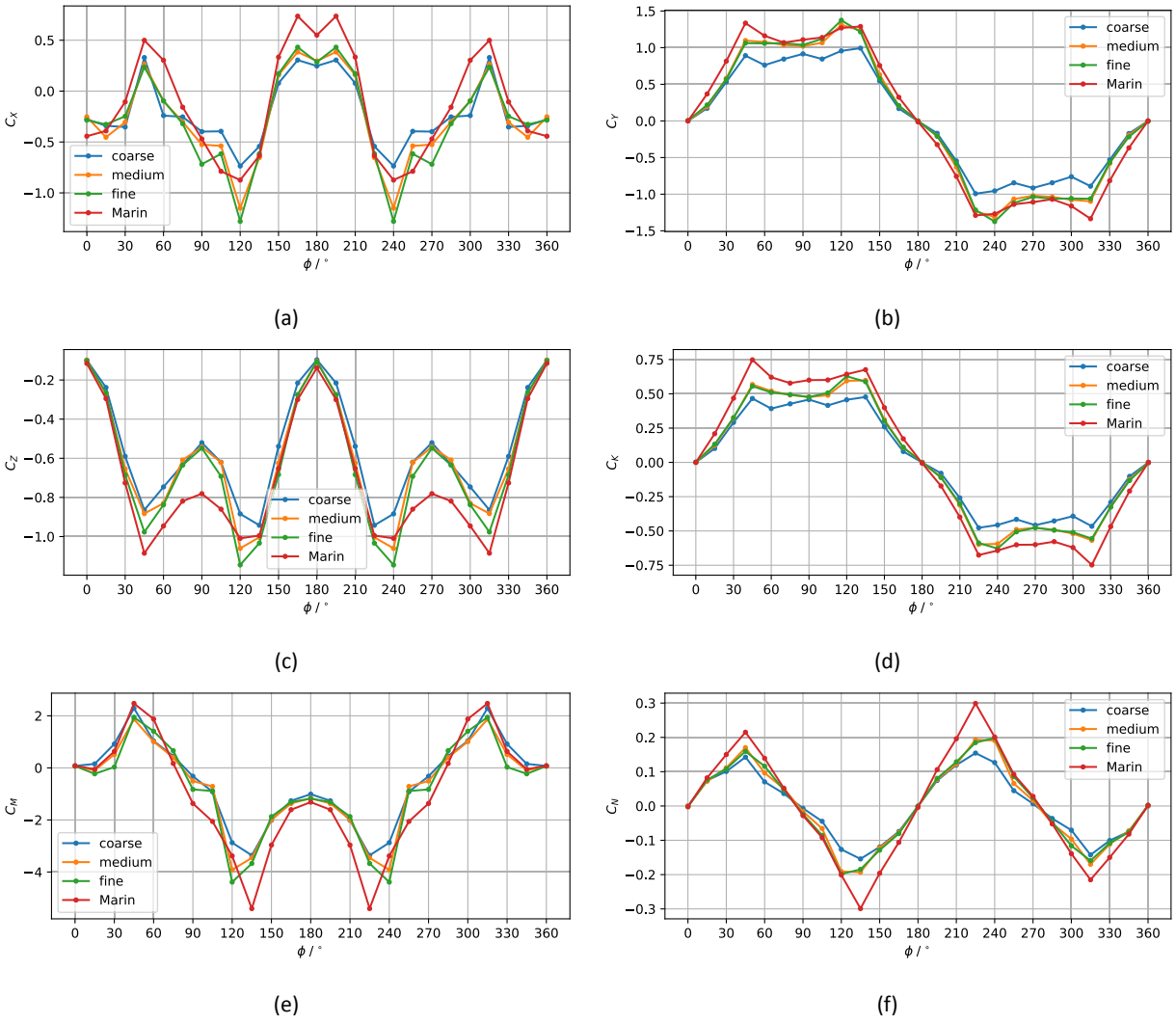

Figure 12 – Influence of the maximum refinement level on the hull and in the wake on the wind coefficients.

The graph of the computing time as a function of the φ (Fig. 13) shows that for a maximum refinement level on the hull of 10 and 11 (which corresponds to the coarse and medium computations), the computing time is always less than a day. The computations with 12 refinements on the hull (fine), show a significant increase in computing time (seven days), especially for the wind angles $50° <= \varphi <= 120°$ (which were run for four seconds – twice as long as the other angles – to ensure sufficient convergence of the integral quantities).

Given the small difference between the medium and fine computations visible in most of the graphs in Fig. 12 combined with the significant increase in computing time for the fine computations as compared to the medium computations, it is decided to execute any further computations with the same refinement settings as used for the medium computations ($N_s = 11$ and $N_w = 9$).

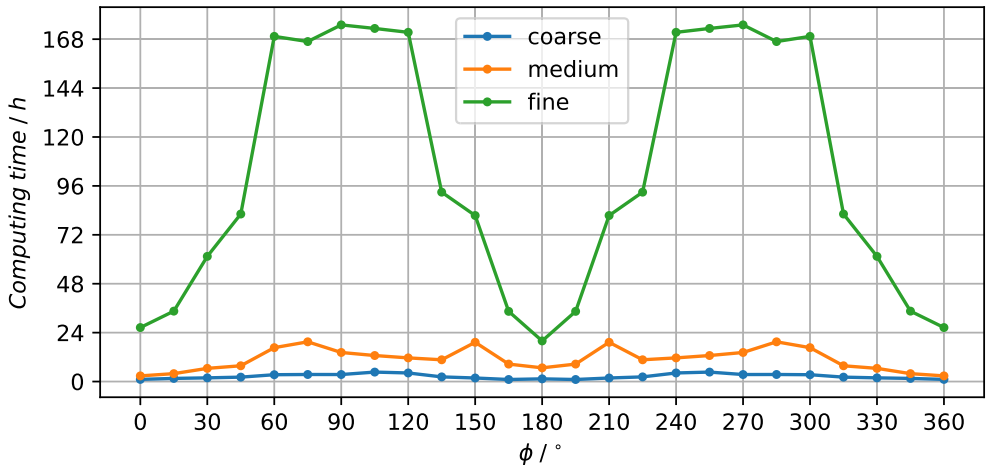

Figure 13 – Computing time as a function of wind angle for the coarse, medium and fine computations.

3.3 Wind angle spacing

The set of computations is split in two, with $\Delta\varphi_1 = 15°$ and $\Delta\varphi_2 = 10°$. The resultant force components are shown in Fig. 14 as a function of the wind angle φ. The differences in the results between $\Delta\varphi_1$ and $\Delta\varphi_2$ are in general not large, except at locations in the graphs where a peak in the value is attained. One notable example is found near $\varphi = 50°$ for C_X and C_Z, where the result with $\Delta\varphi_1 = 10°$ predicts an extrema with a significantly higher value than the extrema for $\Delta\varphi_1 = 15°$. Hence, a smaller increment between the discrete wind angles will increase the likelihood of finding extrema in the graphs. This is also the case for the results of Marin, the peak value of C_X near $\varphi = 45°$ may be lower than the value at $\varphi = 50°$. Finding theses extremes is especially important when a linear interpolation scheme is used to determine coefficient values at wind angles in between the data points. If one assumes that the curves are supposed to vary smoothly between data points, a (cubic) spline interpolation may be a better choice.

For the current research, a wind angle increment equal to $\Delta\varphi = 15°$ is considered sufficient and used for all further computations.

3.4 Partial coefficients

All six partial coefficients for case 3S2L are shown in Fig. 16 for each of the coefficients. Some observations about the contributions of the different parts are given below for each of the six force components.

For the other hull divisions as listed in Table 2, the graphs are shown in Appendix A1.

3.4.1 C_X

The middle section on the bottom layers (S2L1) does not contribute to C_X, since it does not have any surface parts normal to the X-direction. Part S2L2 above it, does not contribute much either, the majority comes from the first and last sections located at the stern and bow, respectively. For $\varphi = 0°$, the major contribution comes from the aftmost section (S1L1 and S1L2), followed by the the lower part of the front section (S3L1). The front and aft sections behave similarly for small incidence angles: both front sections (S3L1 and S3L2) have a peak at $\varphi = 45°$ with a gradual decrease for higher angles, while the aft sections (S1L1 & S1L2) have a peak value at

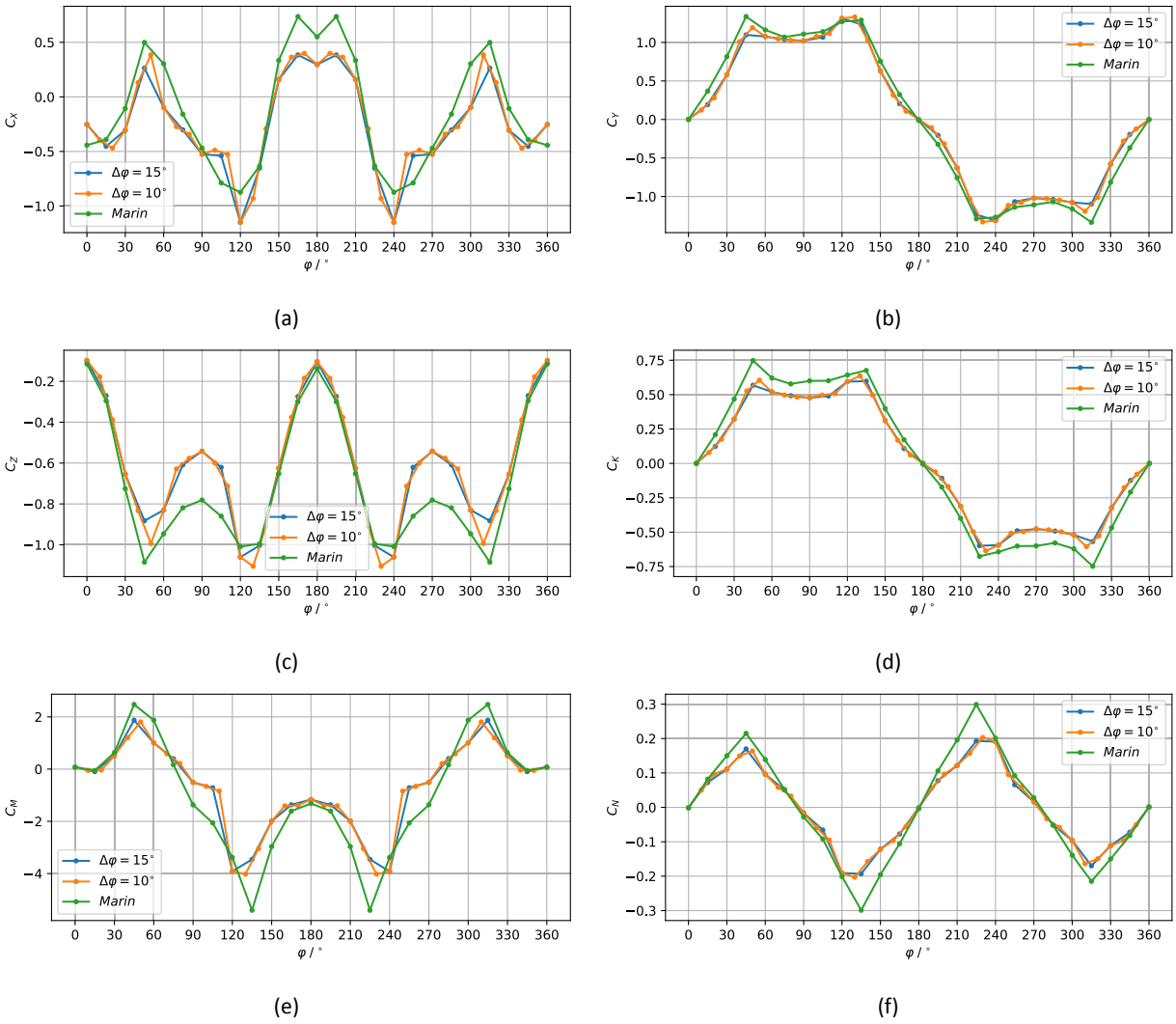

Figure 14 – Influence of the maximum refinement level on the hull and in the wake on the wind coefficients.

$\varphi = 120°$ (which corresponds to an incidence of $60°$ from directly aft) and steadily decreasing values for lower values of the wind angle φ. For a head-on (or tail-on) wind, the resulting drag coefficient value is highest for wind from behind, which should be the case since the front part of the superstructure has a more streamlined shape that the aft part of the superstructure. For $\varphi = 120°$, Fig. 15 shows the pressure distribution on the hull, the velocity magnitude on the domain bottom and velocity vectors in a horizontal plane halfway between the hull deck and the domain bottom. This shows a large low-pressure region on the rounded stern caused by the attached flow. This results in a significant contribution to the longitudinal hull force, that is likely an overestimate of reality. Without the rounded surface, the peak value in C_X at $\varphi = 120°$ would be either not be present or significantly lower.

3.4.2 C_Y

At $\varphi = 90°$, the lower part of the middle sections has the biggest contribution to the lateral force C_Y. The contribution of the upper part of the middle section as a function of the wind angle is similar to the lower part: an almost linear increase from head-on wind to $60°$ connected with a fairly constant contribution for the angles between $60°$ and $120°$. Similar to the longitudinal force C_X, the front and aft sections show symmetric behaviour with respect to $\varphi = 90°$.

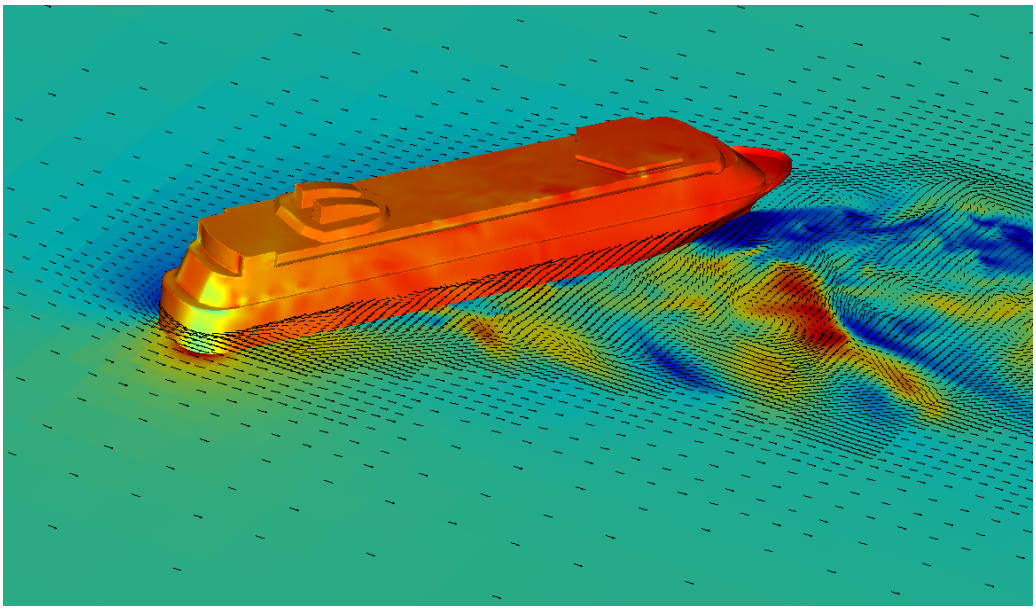

Figure 15 – Pressure distribution on the hull, velocity magnitude on the domain bottom and velocity vectors halfway the lower hull part for $\varphi = 120°$ which shows the extent of the attached flow on the rounded stern. This flow attachment causes a low pressure region that results in a peak value for the longitudinal force.

3.4.3 C_Z

The vertical force C_Z on the hull (negative upward) is caused by the deflection of wind over the hull, resulting in regions with low pressure at the top of the hull. As a consequence, the contribution of the bottom layer to this force is minimal, the top layer contributes most. With respect to the $\varphi = 90°$, the forward and aft section behave similarly, with a peak value close to $45°$ from head-on wind. The middle section follows the trends of the front and aft sections (with maxima at both the aforementioned wind angles), although the contribution is near zero for the head wind and tail wind.

3.4.4 C_K

The trends of the roll moment C_K are very similar to the trends of the lateral force C_Y, with the biggest difference that now, the relative contribution of the top parts is higher due to the longer arm of the lateral force with respect to the reference point (located on the waterline).

3.4.5 C_M

The pitch moment C_M mainly consists of counteracting contributions from the upper parts of the front and aft sections (S1L2 and S3L2): the other four parts do not contribute significantly.

3.4.6 C_N

The main contributions for the yawing moment C_N come from the four parts comprising the front and aft sections, the middle sections contribute very little since due to their almost zero moment arm with respect to the ship's reference point. Similar to the contributions to the longitudinal force C_X, the middle section does not add significantly to the total yawing moment. The bottom parts of the longitudinal extremes dominate

the contribution, with similar trends for the upper parts of these sections, but with lower magnitudes due to smaller areas. The result is a yawing moment that consists of a curve with three sections (two extrema) where the trend changes almost linearly as a function of φ.

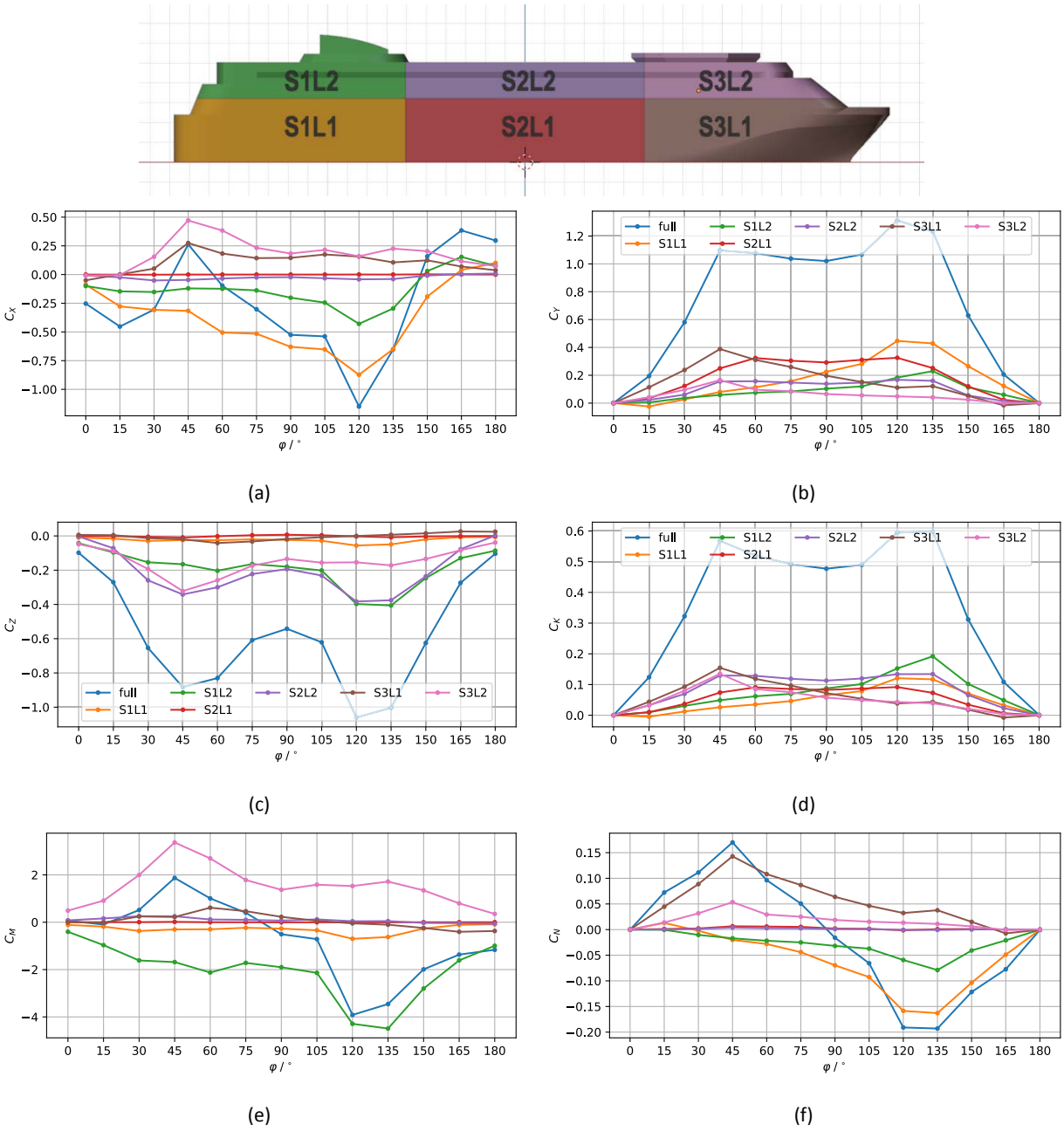

Figure 16 – Contribution of the partial coefficients to the total value for case 3S2L with three sections and two layers.

3.4.7 Conclusions

Overall, the trends of the different partial coefficients are all fairly obvious. For the longitudinal force C_X, the pitching moment C_M, and the yawing moment C_N the total value consists of partial contributions that counteract each other, which can have a significant impact on the location of extrema and zero-crossings.

3.5 Alternative stern geometries

Extra computations are executed with the medium refinement settings for the two alternative stern geometries. The force and moment coefficients are shown in Fig. 17 for the alternatives and the original ship geometry. Significant differences can be observed for the longitudinal force C_X (Fig. 17a) for almost the complete range of wind angles, whereas for the other force components, differences (if any) are less pronounced. For C_Z, C_M and C_N (Figs. 17c, 17e and 17f, respectively), the largest difference between the original and alternative geometries is found for $\varphi = 120°$. For this angle, instantaneous flow visualisations of the velocity (on the domain bottom) and pressure on the hull near the stern are shown in Fig. 18 for the three stern geometries. The low-pressure region that is observed with the original stern is not present with the straight stern: flow separates from the upstream edge resulting in an almost constant pressure on the stern face. The flow separation on the lower stern affects the pressure distribution on the rounded stern section located above, where the low-pressure region is not as pronounced. Geometrically, the chamfered stern is closest in shape to the original stern geometry. As a result, the pressure distribution and velocity fields are in between results of the original and straight stern geometries.

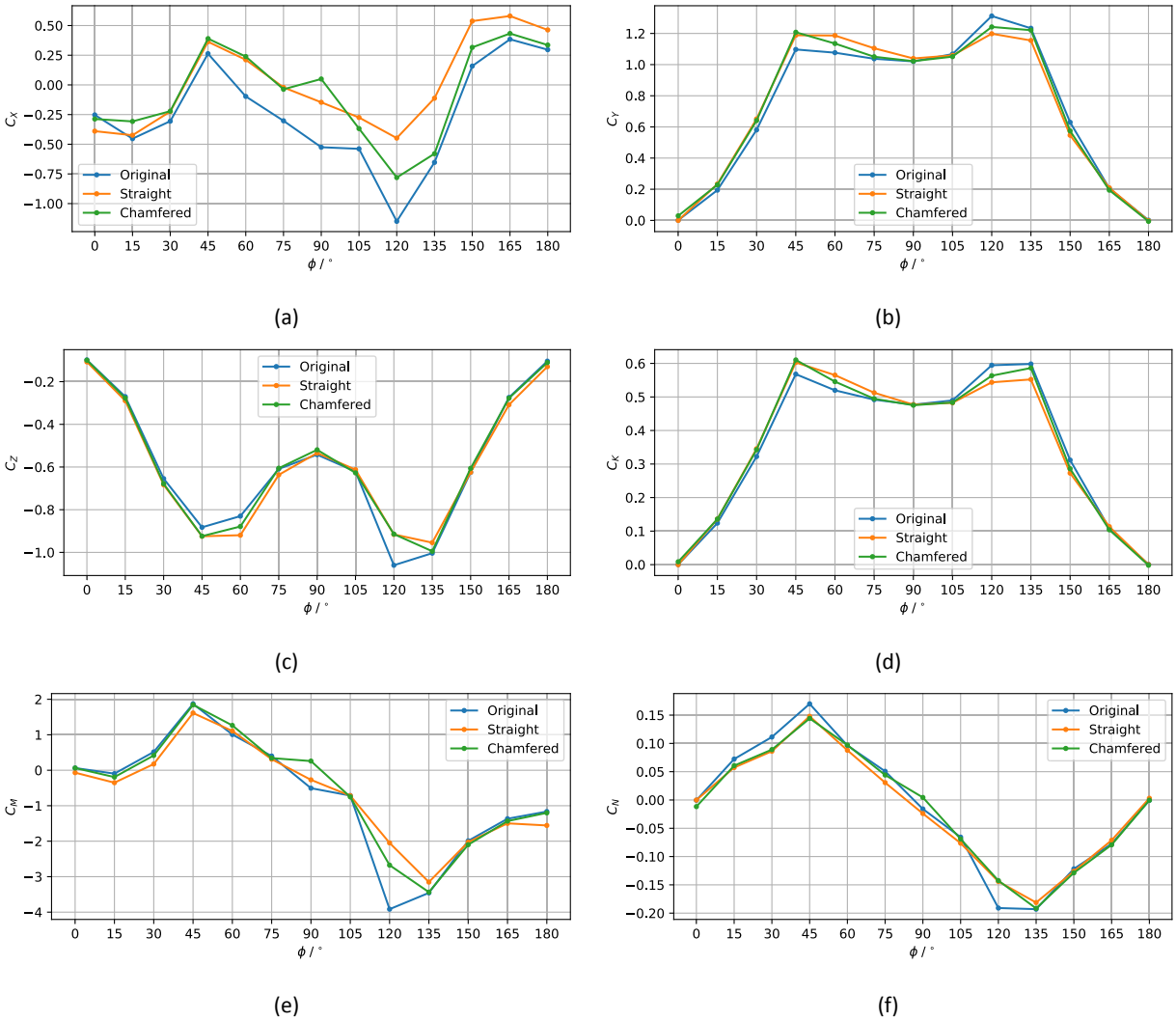

Figure 17 – Comparison of the forces and moments on the windlass cruise ship between the original and modified stern geometries.

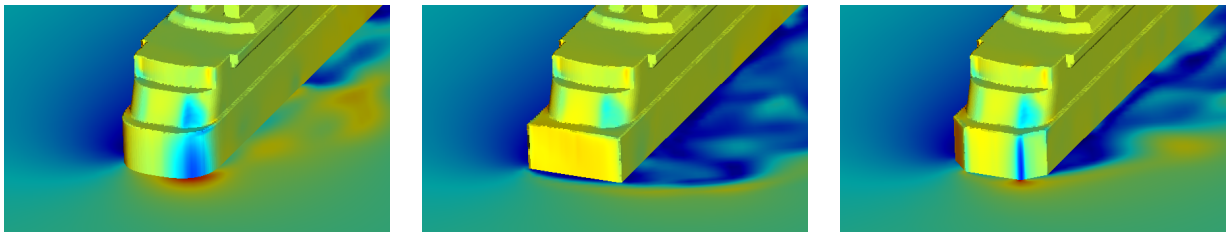

(a) Original stern. (b) Straight stern. (c) Chamfered stern.

Figure 18 – instantaneous pressure distribution on the stern of the hull and velocity magnitude on the domain bottom for the original and modified stern geometries.

This comparison shows that without altering the frontal and lateral silhouettes of a ship, the particular stern geometry can have a profound influence on the magnitude of the longitudinal hull force. This also means that one should be careful when selecting wind coefficients from literature (e.g. as found in Blendermann (2013, 1993)) for a similar vessel in the simulator when only frontal and lateral silhouettes of the vessels tested in the wind tunnel are shown. It is not because the silhouettes are similar (or the same), that this automatically means that the experimentally obtained wind coefficients are suitable: the devil is in the details.

4 Simulation results

In this chapter, results are shown of simulations where partial wind coefficients are used to compute the forces experienced by a ship subject to both vertical gradients in the wind field and horizontal gradients in the wind field. The setup of these computations has been discussed in § 1.5. It should be noted that simulations are only executed with the original hull geometry and not with the two alternative stern geometries.

When simulating vertical wind gradients, the number of longitudinal sections in which the hull is partitioned does not matter; only the number of layers affects the results, while for the case of a horizontal gradient, only the number of longitudinal sections matters.

In both cases, the results will depend highly on the location at which the velocity is sampled for each of the hull parts. Two options are investigated here. For the first one, the velocity is sampled at the geometric centre of the rectangles that demarcate the areas within which forces are summed in Gerris for the partial coefficient computation. A second option uses a number of points uniformly distributed within these areas where, at each point, velocity is sampled and an average is computed.

4.1 Vertical gradient

Results for this case are stationary: no time simulations are executed. The total force is computed by summing the results of the different parts, and these results are again made dimensionless (using the reference velocity ($V_\infty = 25\,\mathrm{m/s}$) at the reference height of $10\,\mathrm{m}$) to get equivalent coefficient values for each of the six force components. As such, a direct comparison can be made with the wind coefficients computed by Marin and the full coefficients computed with Gerris assuming uniform flow.

First, all coefficients are shown for case 5S3L in Fig. 19. This includes the coefficients as computed by Marin assuming an atmospheric profile, the full values computed with Gerris assuming a uniform velocity field, and the coefficients obtained assuming the two velocity profiles as shown in Fig. 6. For each of the latter two profiles, two sets of coefficients are computed, where the differences are due to the choice of the reference point where the velocity is sampled. The labels that contain *geom.* were computed by sampling the velocity at the geometric centre of each of the rectangular areas used for the hull divisions (shown in Fig. 32 for the current case), while the labels that contain *avg.* were computed by averaging the velocity at 32 points linearly distributed between the lower and upper boundaries of each hull part. The former option (*geom.*) is the lower extreme of uniformly distribution points, which is what one would normally do in potential panel methods.

Note that the actual shape of the hull is not taken into account when sampling velocities: it is possible that for hull parts in the top layer, the uppermost sampling points are located above the highest point of that hull part. It might be better or more correct to use the silhouette of the ship as boundary for the placement of the sampling points. For now, this is left as a recommendation for the future.

Looking specifically at the results for C_Y (Fig. 19b), it is clear that the vertical division of the hull in layers has the intended effect: the total lateral force C_Y is lowest for the uniform velocity profile, it is higher for the Frøya profile and highest for the *port* profile. This is also observed with the five other components. For a ship with a superstructure height that is close to the reference height where the velocity is defined, the effect is the opposite: both atmospheric profiles result in forces that are significantly smaller than the forces obtained using a uniform velocity field. This is shown in Fig. 20, where the results of Marin have been left out because those were computed using $z_{ref} = 10\,\mathrm{m}$. Now, the port profile results in the smallest forces on the hull,

the force components for the Frøya are somewhat higher, and both of these are significantly smaller than the coefficients assuming a uniform velocity field.

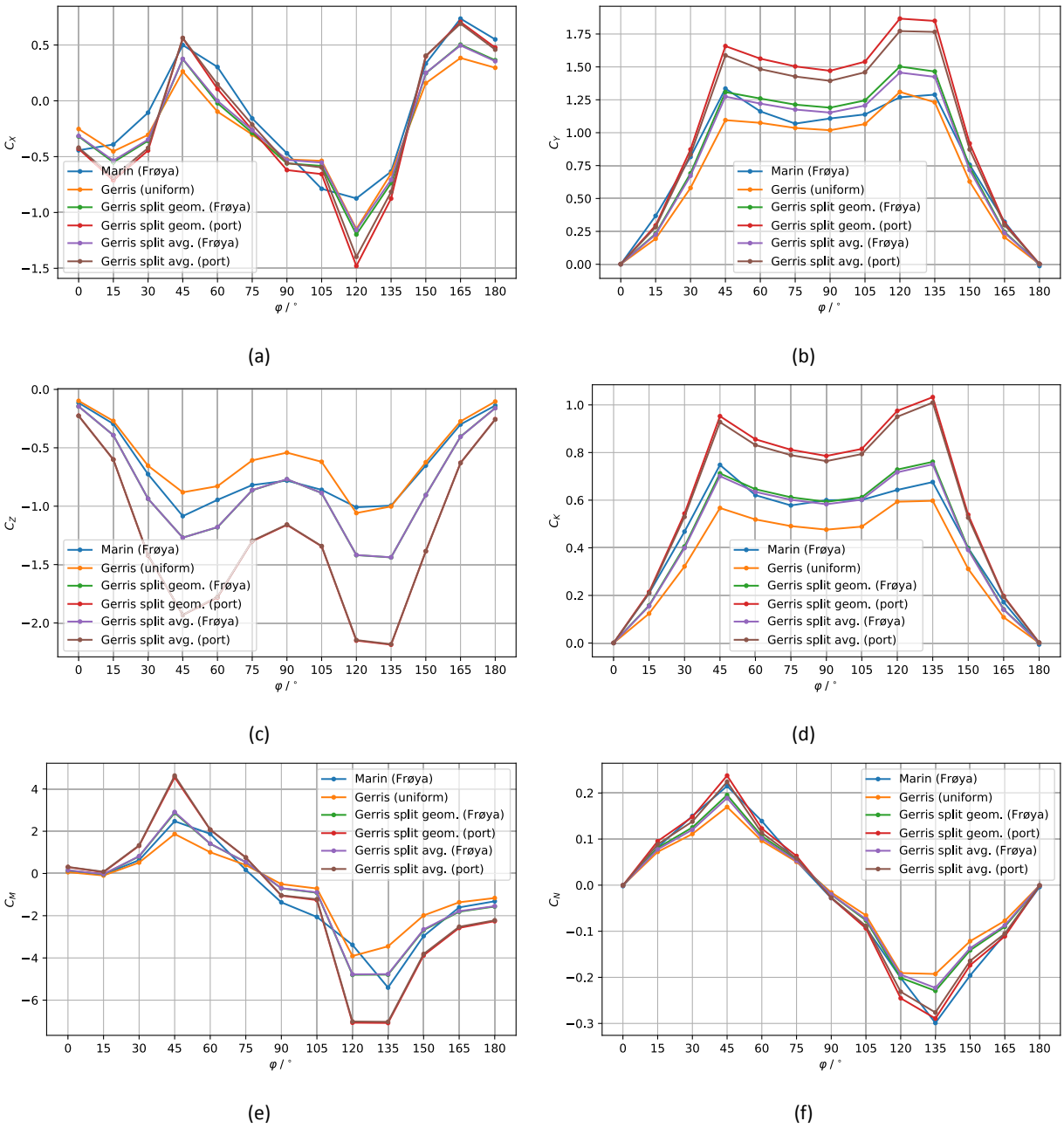

Figure 19 – Comparison of wind coefficients for the cruise ship for two atmospheric profiles ($z_{ref} = 10$ m).

For the location of the reference point, using a single point at the geometric centre of the hull parts always gives higher forces as compared to using an average velocity. This is caused by the specific shapes of the atmospheric velocity profiles: the value at the geometric centre of a vertical section is always larger than or equal to the average velocity over that vertical section.

For the lateral force component C_Y using the Frøya profile, convergence of the coefficient value as a function of the number of points used for velocity averaging is visualised in Fig. 21 both using absolute numbers and using relative errors. Note that for the reference value used in the computation of the relative errors, the results with the highest number of points (32) are used, the relative errors of which are left out because they are exactly zero. For both $\varphi = 0°$ and $\varphi = 180°$, the relative errors have been discarded as well because the reference value is very close to zero and as a consequence, the relative error can become arbitrarily large. When four

points or more are used to compute a velocity average over the height of a layer, the error is smaller than $1\,\%$. With four points, the vertical distance between the points is still four meter. For this type of smooth velocity profiles, four to eight points per layer are probably enough, but if a more random velocity profile would be used, more points might be required to compute an accurate average.

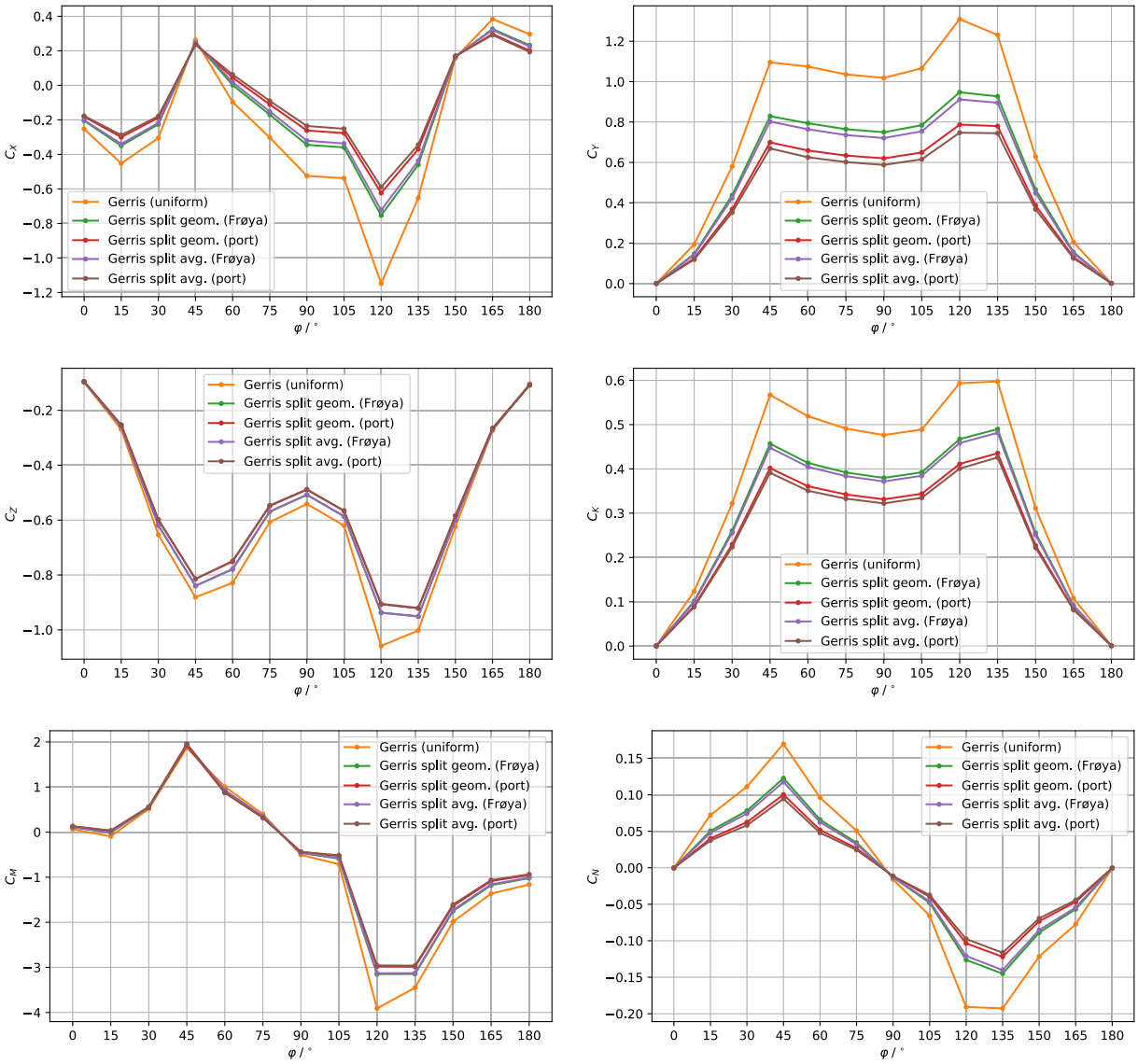

Figure 20 – Comparison of wind coefficients for the cruise ship for two atmospheric profiles ($z_{ref} = 60\,\text{m}$).

The influence of the number of layers in which the hull is subdivided in the CFD computations on the ability of the current method to account for vertical wind gradients is simulated for the case of the Frøya velocity profile using hull divisions using one layer, two layers and three layers. These results are displayed in Fig. 22. For these results, the velocity was sampled at 32 points uniformly distributed over the height of each hull layer. The differences between the results using a single layer on the one hand and two or three layers on the other hand is rather large. When two or more layers are used, the differences are almost indistinguishable, with the exception of the vertical force C_Z. It is concluded that for this type of smooth velocity profile, at least two layers are required and three layers are sufficient.

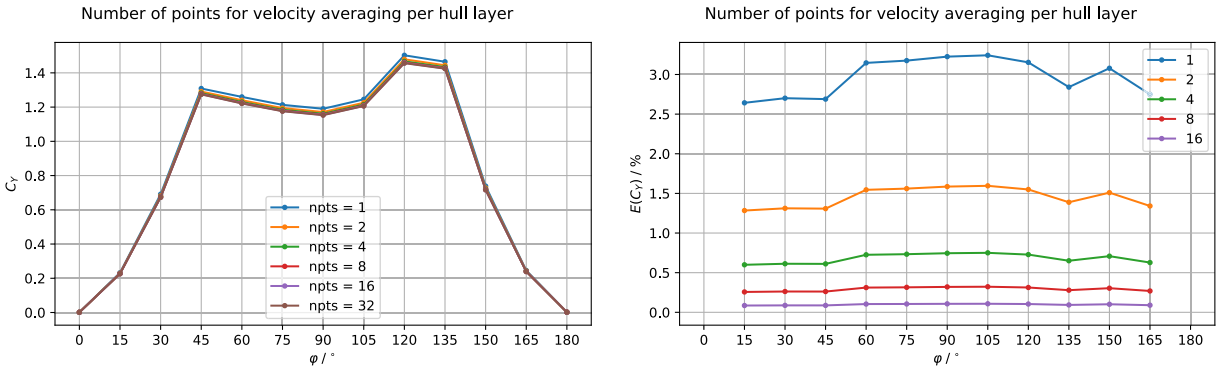

(a) Absolute values. (b) Relative errors.

Figure 21 – Convergence of the lateral force coefficient as a function the number of points used for velocity averaging for different wind angles for the Frøya atmospheric profile: (a) absolute values and (b) relative errors.

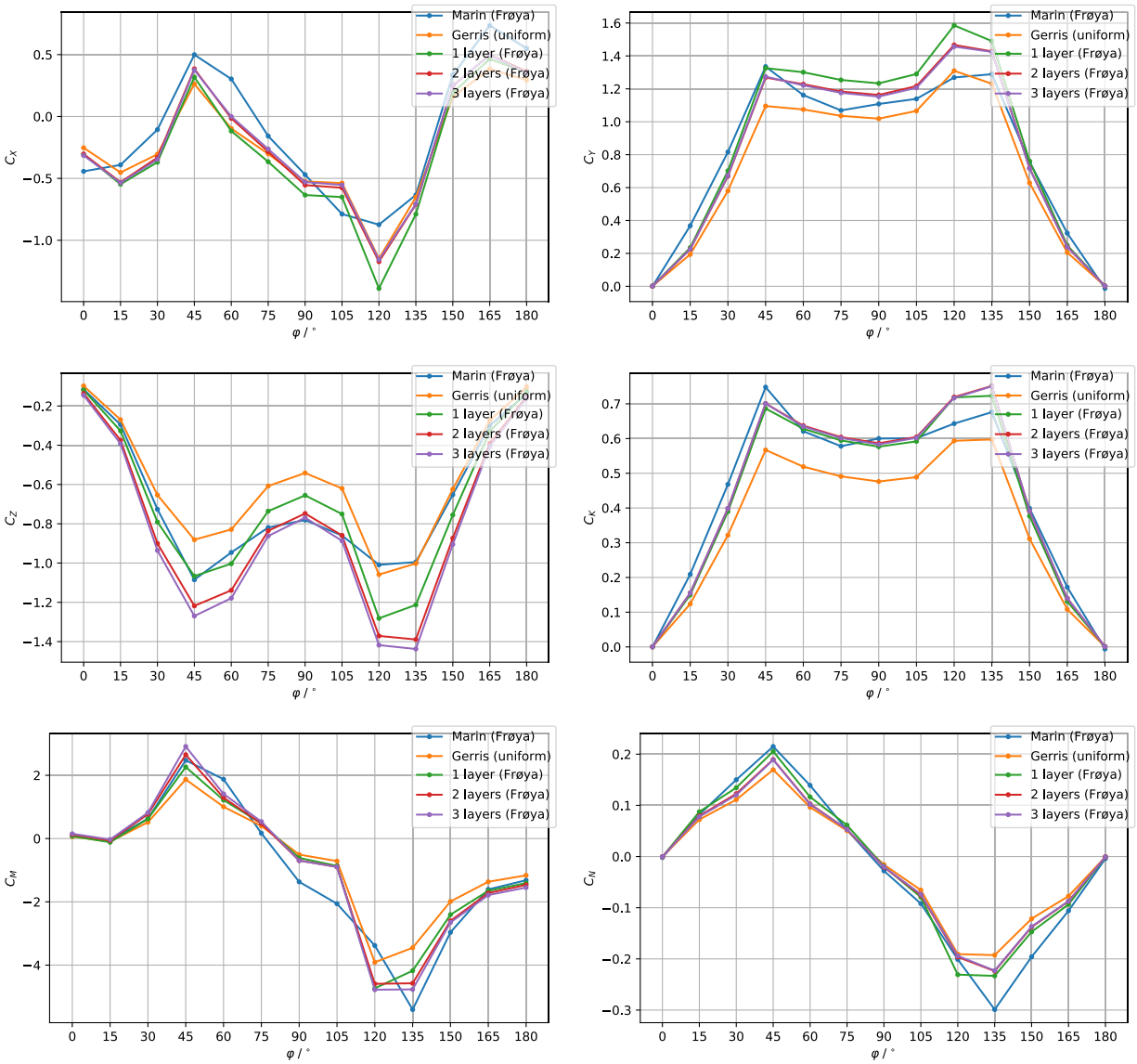

Figure 22 – Comparison of wind coefficients for the cruise ship for the Frøya atmospheric profile as a function of the number of layers.

4.2 Horizontal gradient

For the horizontal gradient, the cruise ship sails with a constant velocity along a straight track in the negative x-direction through a wind field oriented perpendicular to the track of the ship. As noted before, the ship speed is not taken into account in the computation of the wind angle φ. The initial x-position of the cruise ship is $x_0 = -1250\,\text{m}$, the y-position is always zero, its heading is $\phi = 180°$ and its speed along the x-axis is $V_s = 2.5\,\text{m/s}$. Simulations are run for $1000\,\text{s}$ with a time step of $\Delta t = 1\,\text{s}$, hence the final x-position is $x_{end} = -1250\,\text{m}$. With these initial and final positions, the ship is fully *submerged/engulfed* in the wind field (which extends to $x = \pm 2000\,\text{m}$, see Fig. 5). For pure horizontal gradients, only the hull division in sections matters, the vertical division in layers has no influence on the results. For the initial results, the velocity is sampled at 16 points that are uniformly distributed between the boundaries of each hull section.

The time variation of the force coefficients are shown in Fig. 23 for the three wind profiles presented in § 1.5.1 for hull case 5S3L. Some noteworthy observations are that for the force components where the partial contributions all have the same sign (C_Y,C_Z and C_K), the resultant values gradually change from a high value to a value four times smaller. Note that for the *sigmoid+rnd* case, there is a slight reduction in these values before the ship enters the sigmoid gradient (starting at $t \approx 210\,\text{s}$) that is caused by the reduction in the velocity between $x = 250\,\text{m}$ and $x = 730\,\text{m}$ (see Fig. 5). For the other components (C_X, C_M and C_N), which consist of partial coefficients that counteract each other, a local maximum is reached during halfway during the gradient. For the yawing moment C_N, this is fairly obvious: due to high velocity acting on the aft half of the hull and a low velocity acting on the forward half of the hull, the moment arm of the lateral force acting on the hull front half cannot balance the moment arm on the aft part which results in a momentarily larger yawing moment, trying to rotate the hull with the bow into the wind. For the longitudinal force C_X the cause is to be found in the differences in the hull shape at the bow and stern (mainly the lower half): the hull geometry at the bow is pointed, whereas at the stern, it is flat. The difference for the upper parts are smaller: at both ends, the geometry is fairly flat (although slanted aft at the forward end). This shape difference results in a larger area with low pressure at the stern than at the bow (see Fig. 24 for a visualisation of the time-averaged pressure field on the hull and domain bottom). When the velocity at the bow is reduced, the forward part experiences less of a forward suction force, while at the aft end, the forces tries to reduce the ship speed. This results in a temporary increase of the drag force of the hull during the transition. The same holds true for the pitching moment C_M.

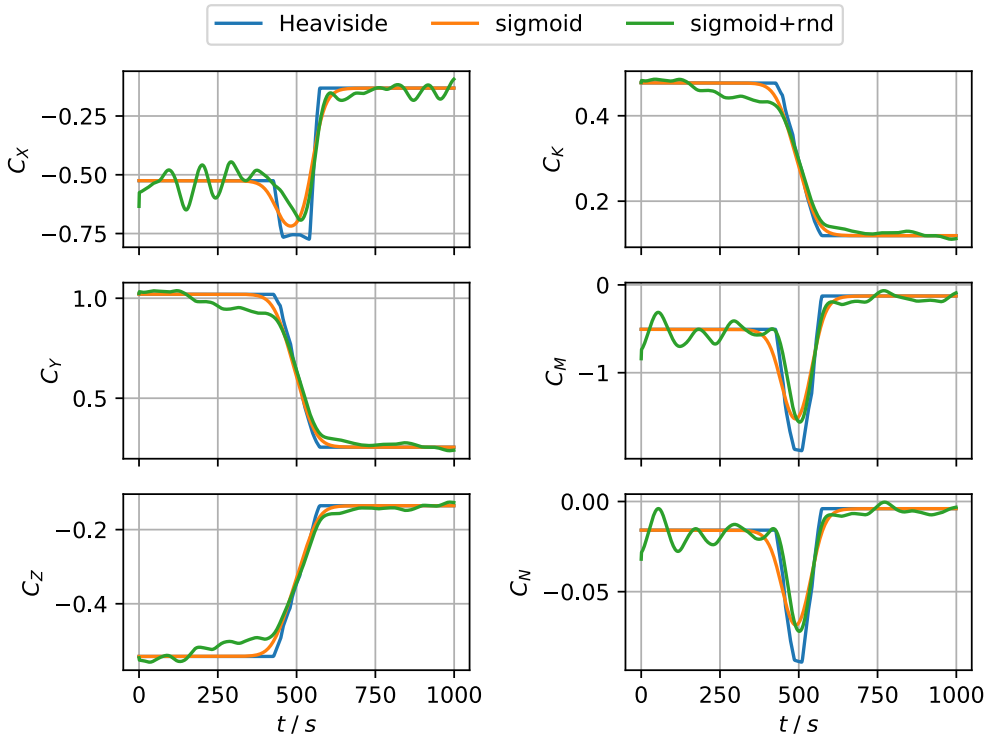

Figure 23 – Time histories of the six force components for the three velocity profiles for case 5S3L (16 points per hull section for velocity averaging).

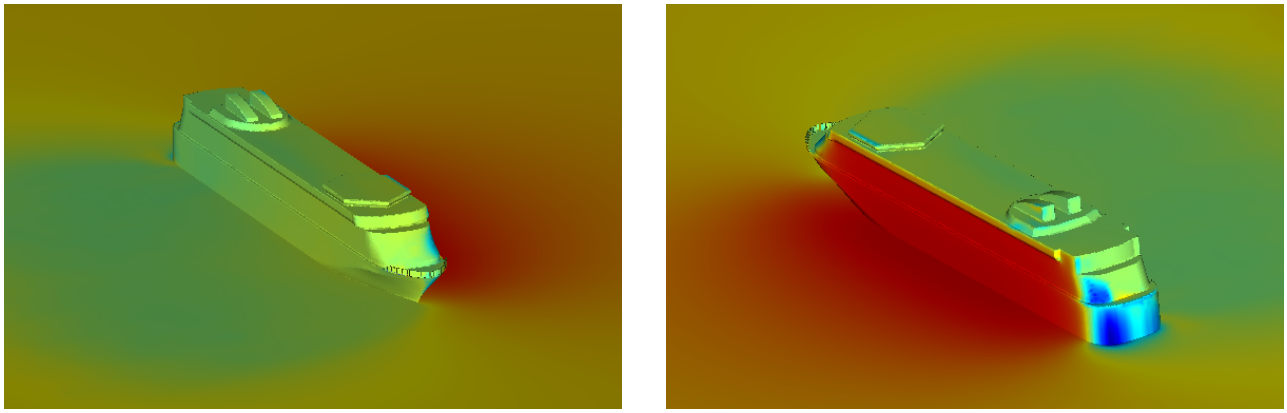

Figure 24 – Visualisation of the averaged pressure field on the hull and domain bottom. Red-coloured areas are high pressure and blue-coloured values are low pressures.

Using the same hull case, but reducing the number of evaluation points per hull segment to one, the time variation of the force coefficients as displayed in Fig. 25 is obtained. For the Heaviside wind field, the differences are significant: during the transition, the total forces on the hull change in discrete steps. For the other wind profiles still a smooth transition is obtained, although the sigmoid with random components does show somewhat larger variations in the amplitude. For the smooth sigmoid wind profile, the response of the hull is still a smooth curve although the peak values for the counteracting force components (C_X, C_M and C_N) are lower.

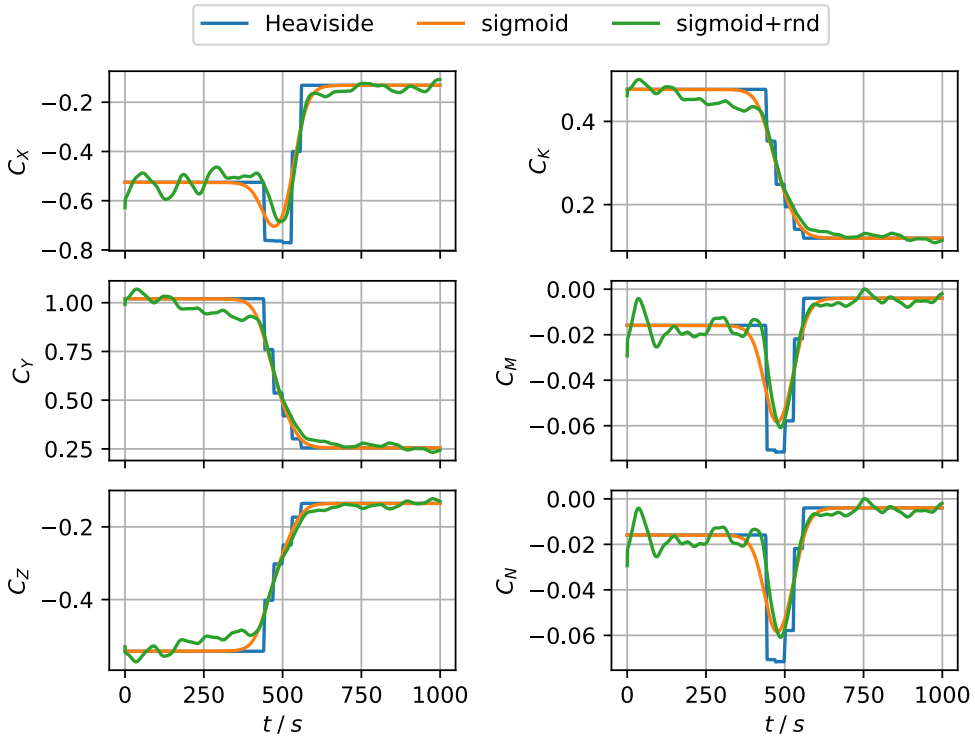

Figure 25 – Time histories of the six force components for the three velocity profiles (Fig. 5) for case 5S3L (1 point per hull section for velocity averaging).

The number of sections in which the hull is divided for the wind coefficient computation has a significant impact on the results. For the *sigmoid* velocity profile, all coefficients are shown for all five cases on an absolute scale in Fig. 26. Similar graphs have been produced for the other two velocity profiles, these are displayed in Appendix A2.1. From the graphs in this figure, it is clear that results converge as the number of sections is increased. Using the result with the largest number of sections as a reference, the relative errors of the other hull divisions are computed and these are displayed in Fig. 27. When using few sections to split the hull forces, the error for the longitudinal force C_X is significant: 20% and higher for 3 sections or less. With four sections, the error drops to five percent. Note that C_X converges slowest: for all other coefficients, the coefficient error when using four sections is smaller than 2% for C_N and C_M, while for the other three components, it is less than 0.5%. One can conclude that dividing the hull in three sections is enough to capture the majority of the (non-linear) physics and that five sections is sufficient for practical purposes.

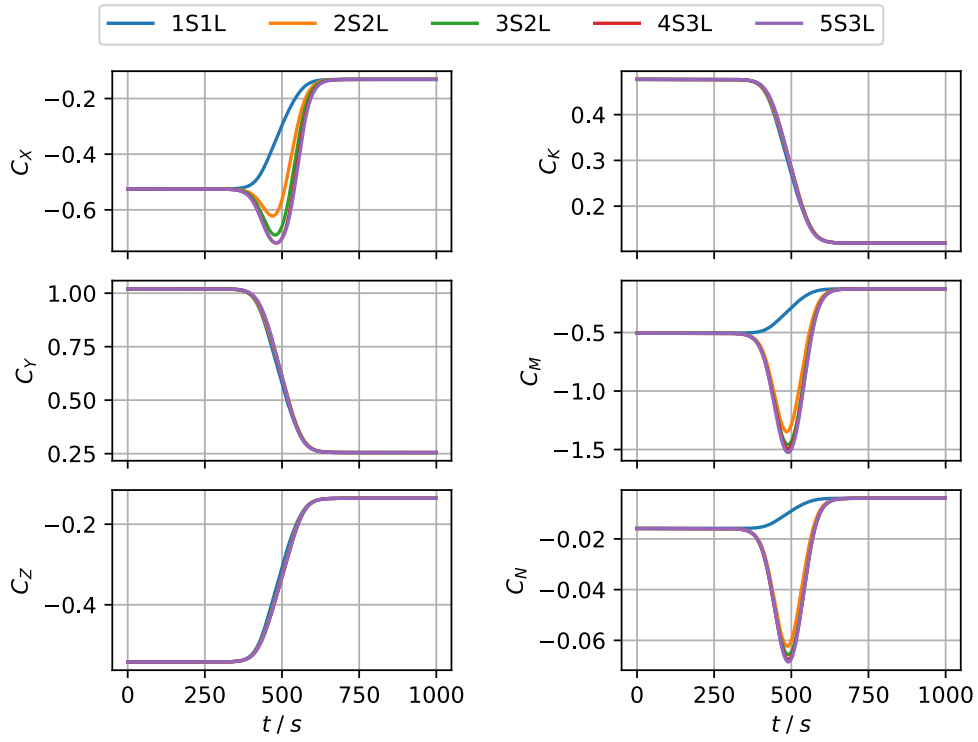

Figure 26 – Time histories of the six force components for the five hull division cases for the simoid velocity profile.

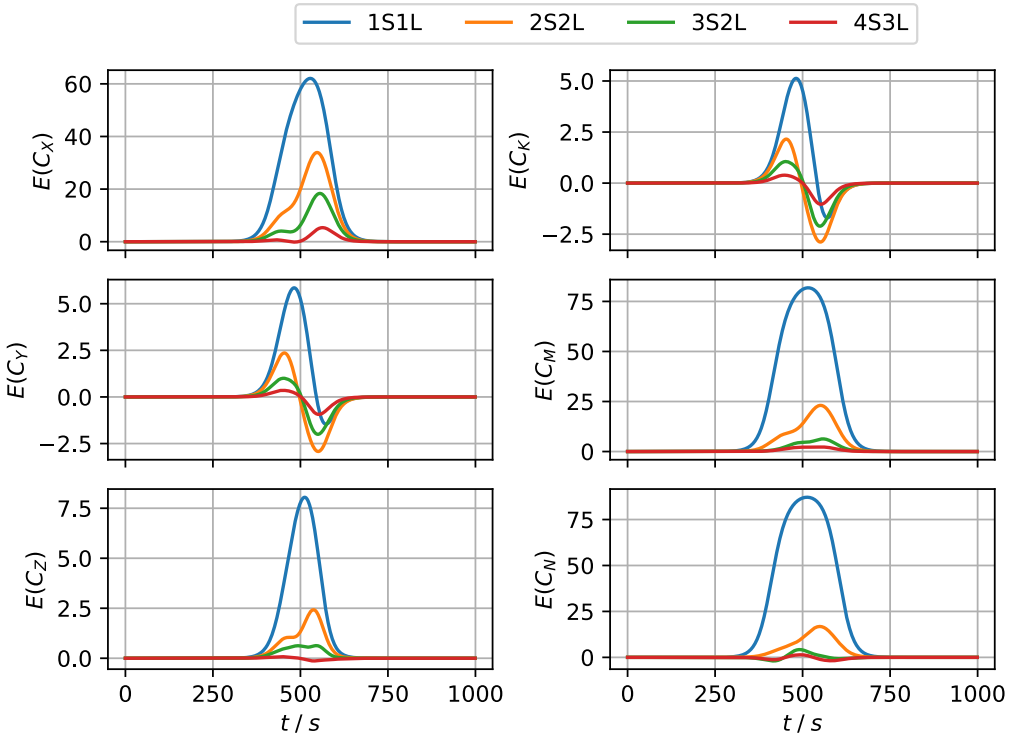

Figure 27 – Relative errors of the time histories shown in 26 using the result of 5S3L as reference.

5 Conclusions and recommendations

In this report, a method is investigated that can account for vertical and horizontal gradients in the wind field in the computation of wind forces and moments acting on a ship in a generic way. Wind coefficients are computed by dividing the hull of a ship vertically in a number of layers and longitudinally in a number of sections. For each of these parts, partial coefficients are determined from the pressure distribution on the hull as obtained with CFD. For the current investigation, horizontal and vertical gradients are treated separately. For a number of representative vertical velocity profiles, the total forces and moments on the ship are determined by computing a representative velocity value for each of the hull parts. For the vertical gradients that were investigated, dividing the hull in three layers is sufficient. Horizontal gradients in the wind field are investigated by advancing the ship from an area with a high lateral velocity field into an area with a low lateral velocity field. At least two sections are required to observe non-linear trends for C_X, C_M and C_N during the transition of the gradient. By increasing the number of sections, differences between the results reduce significantly. When an odd number of sections is used, the peaks of the non-linear transition are wider and more pronounced. Using five sections should be sufficient for practical purposes.

The location of the reference point where velocity is sampled to compute dimensional forces from the partial coefficient value has a significant impact on the results: using a single point per layer for wind velocity profiles typical in ship simulations results in an overprediction of the velocity and hence an overprediction of the resultant force components. Averaging over a number of points uniformly distributed between the bottom and top of the layers, results in a better agreement with the CFD results of Marin. The same holds true for horizontal gradients in the wind field: increasing the number of points results in a smoother time variation of the force components. Although horizontal and vertical wind field gradients have not been combined in simulations, there is no inherent restriction that this would not work as expected. The velocity field should be sampled at points distributed uniformly in a two dimensional grid instead of using points on a line which is sufficient for simulating a single gradient in the wind field. It might be useful to restrict the point locations to the lateral silhouette of the ship, to ensure that velocity is only sampled inside the ship silhouette, and not above it.

It is recommended to implement the current method in the ship simulators at FH. To do so, work is required in various areas related to the simulators:

- partial wind coefficients should be computed for a number of ships;
- a suitable XML format must be determined to store these partial coefficients;
- definition of the parts and the number and location of query points;
- routines must be created to read the data from the input files;
- the routines that currently compute the wind forces and moments must be amended to cope with the computation of partial coefficients next to the current method, or, the new method should be able to cope with full coefficients (one section and one layer).

Although not a trivial task, the author believes it is neither insurmountable and may result in a significant improvement over the currently available method.

The research focus can then turn to the generation and modification of the wind field itself, where a method could be devised that can locally alter the global wind field around (moving) objects in the simulator (such as other ships) in a generic way. One way this could be done is by computing the wind field around a number of objects in CFD and generating a parametric model of the changes induced by the object on the background wind field.

The wind coefficient comparison between the original and alternative stern geometries shows that a particular stern geometry can have a profound influence on the magnitude of the longitudinal hull force. This means

that one should be careful when selecting wind coefficients from literature for a similar vessel in the simulator when only frontal and lateral silhouettes of the experimental vessel geometries are shown. It is not because the silhouettes are similar (or the same), that this automatically means that the experimentally obtained wind coefficients are suitable: the devil is in the details.

References

Andersen, **I. M. V.** (2007). Vindkræfter på Containerskibe. (M.Sc. thesis). Institut for Mekanik, Energi og Konstruktion, Danmarks Tekniske Universitet

Andersen, **I. M. V.** (2013). Wind loads on post-panamax container ship. *Ocean Engineering 58*: 115–134. DOI: https://doi.org/10.1016/j.oceaneng.2012.10.008

Andersen, **O. J.; Løvseth**, **J.** (2006). The Frøya database and maritime boundary layer wind description. *Marine Structures 19 (2-3)*: 173–192. DOI: https://doi.org/10.1016/j.marstruc.2006.07.003

Blendermann, **W.** (2013). Practical ship and offshore structure aerodynamics. Hamburg University of Technology: Hamburg, Germany. ISBN: 978-3-89220-669-9

Blendermann, **W.** (1993). Schiffsform und Windlast-Korrelations- und Regressionsanalyse von Windkanalmessungen am Modell. 533. Hamburg, Germany

Det Norske Veritas (2014). Environmental Conditions and Environmental Loads. DNV-RP-C205. Oslo, Norway

Hosker Jr., **R. P.** (1984). Atmospheric Science and Power Production. ***in:*** Randerson, D. (Ed.). DOE/TIC-27601. United States Department of Energy Technical Information Center: Oak Ridge, TN. Chap. Flow and Diffusion Near Obstacles. DOI: 10.2172/6503687

Pietersma, **M.; Schrijvers**, **P.** (2021). WINDLASS JIP (2019-2022). WP4: CFD wind load calculations for five large ships. Report No. 31273-1-CPO. Wageningen, The Netherlands

Van Hoydonck, **W.; Verwilligen**, **J.; López Castaño**, **S.** (2022). Evaluation of Gerris flow solver for the computation of wind coefficients. Parameter variations and validation. Version 2.0. *FHR Reports*, 16_058_2. Antwerp, Belgium

A1 Additional visualisations of partial coefficients

In this appendix, the partial coefficients for the other hull divisions shown in Table 2 are presented. For each of the cases, a side view of the hull is shown with the hull division visualised using the same colours as used in the graphs.

For C_X, C_M and to a lesser extend C_N, the total value consists of contributions that counteract each other. For the lateral force C_Y, the vertical force C_Z and the roll moment C_M, the contributions of the total value consists of contributions with (mostly) the same sign.

A1.1 2S2L

The division of the hull with two sections (front and aft) and two layers (bottom and top) is shown in Fig. 28. The partial coefficients for this case are displayed in Fig. 29.

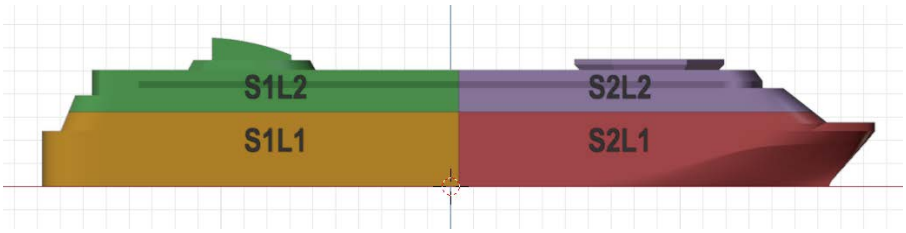

Figure 28 – Sideview of the hull of the WINDLASS cruise ship REF divided in two sections and two layers.

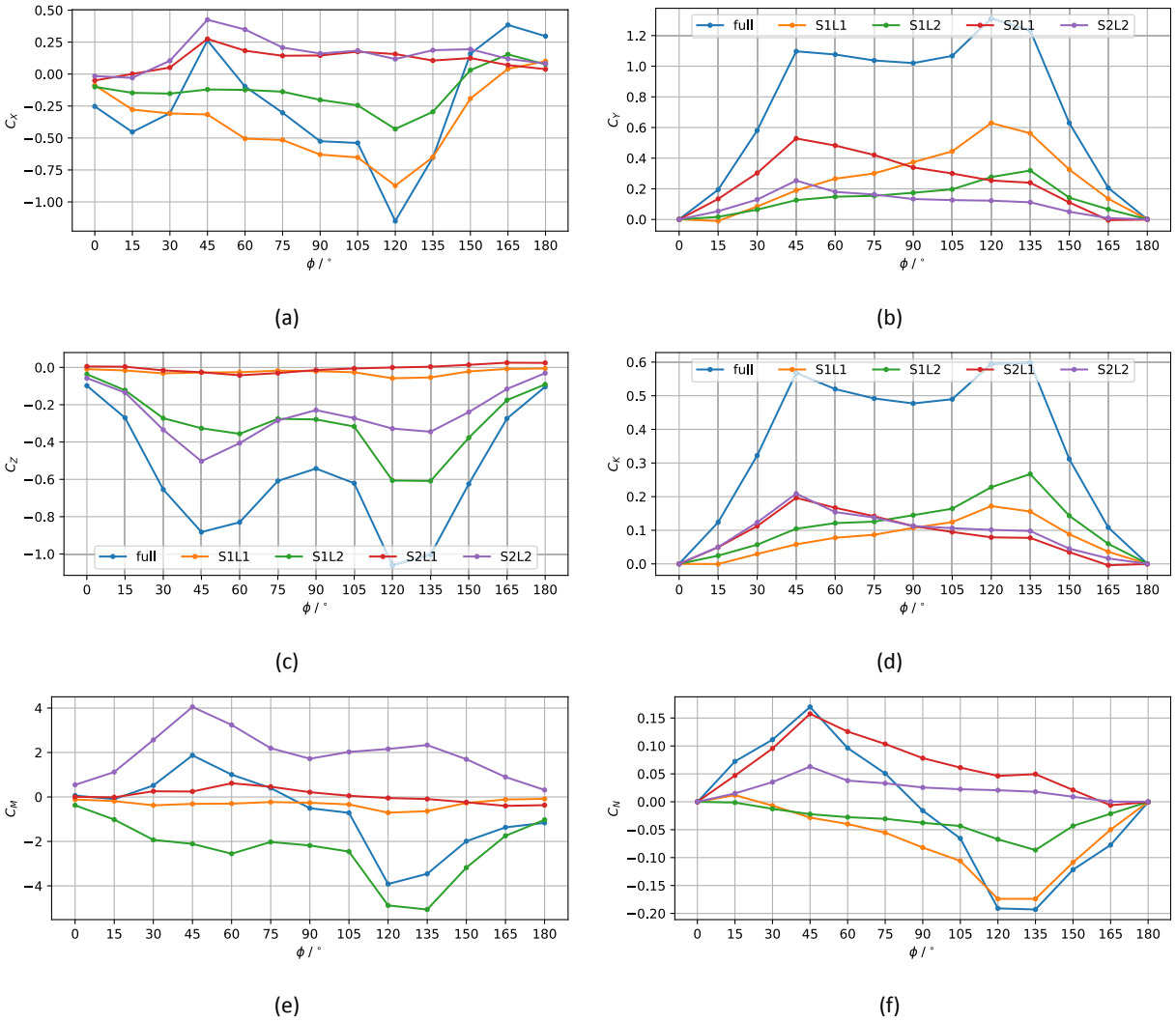

Figure 29 – Contribution of the partial coefficients to the total value for case 2S2L with two sections and two layers.

A1.2 4S3L

The division of the hull with four sections and three layers is shown in Fig. 30 and the contributions of each hull part to the different coefficients is visualized in Fig 31.

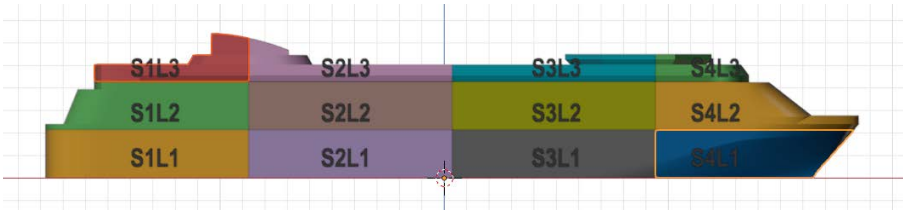

Figure 30 – Sideview of the hull of the WINDLASS cruise ship REF divided in four sections and three layers.

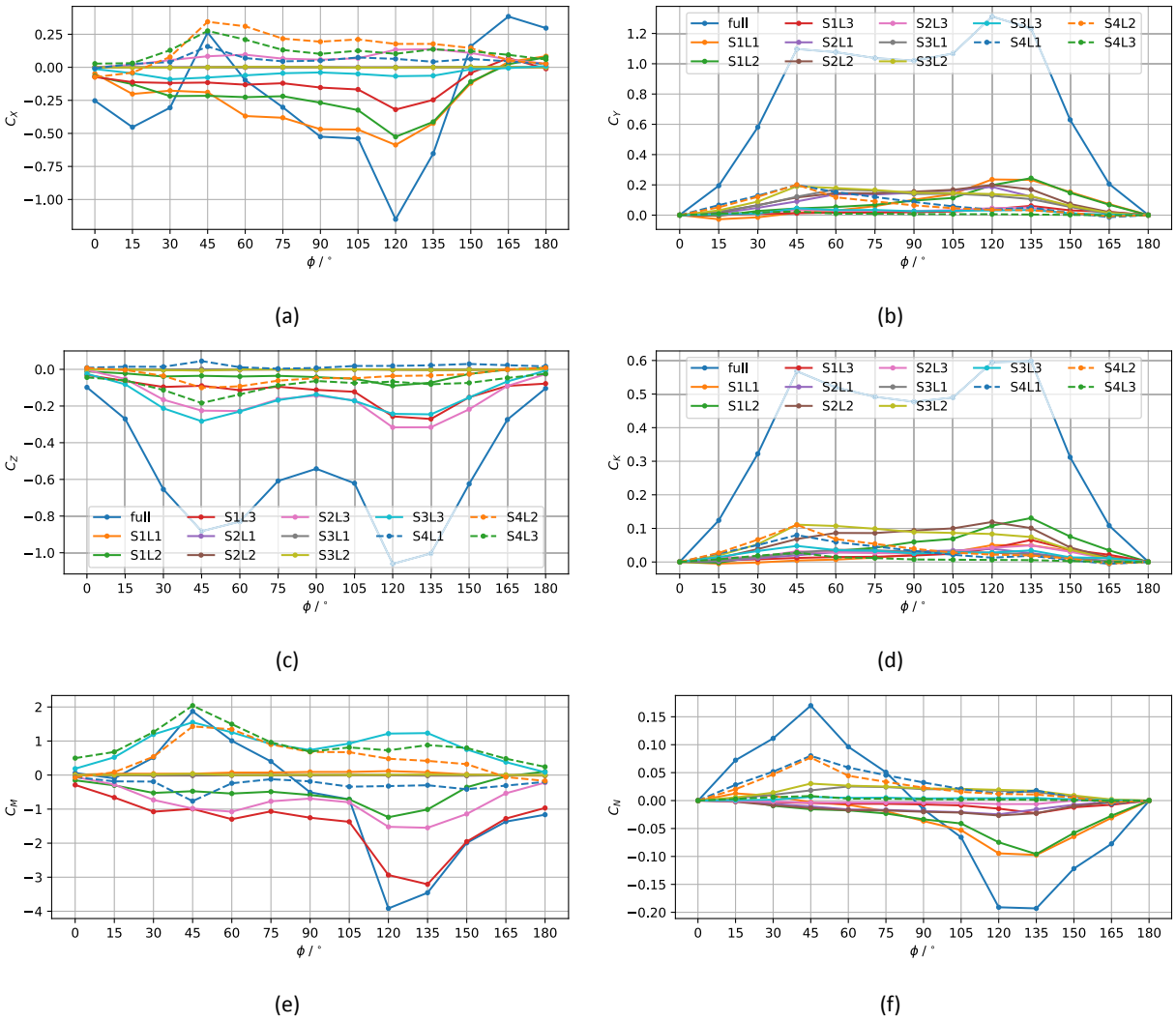

Figure 31 – Contribution of the partial coefficients to the total value for case 4S3L with four sections and three layers.

A1.3 5S3L

The division of the hull with two sections (front and aft) and two layers (bottom and top) is shown in Fig. 32 and the contributions of each hull part to the different coefficients is visualized in Fig 33.

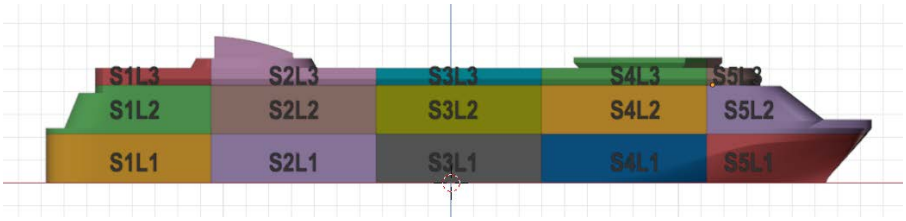

Figure 32 – Sideview of the hull of the WINDLASS cruise ship REF divided in five sections and three layers.

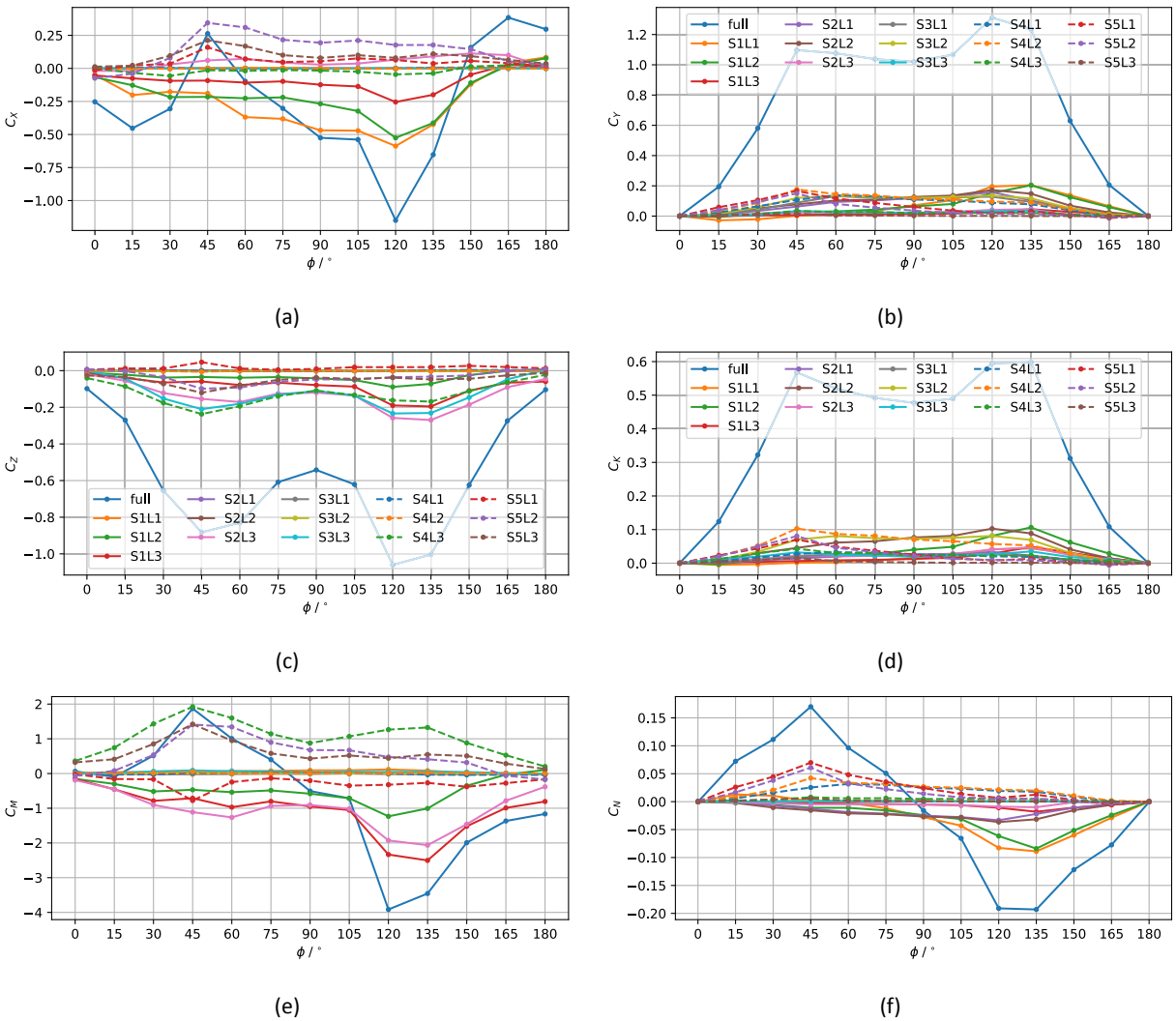

Figure 33 – Contribution of the partial coefficients to the total value for case 5S3L with five sections and three layers.

A2 Additional simulation results

A2.1 Horizontal gradient simulation results

The simulation results for the sigmoid wind profile with random fluctuations for the different hull division cases are shown in Fig. 34 and the relative errors relative to case 5S3L are displayed in Fig. 35. Note that for C_M and C_N at $t = 750\,\mathrm{s}$, the curves almost cross the zero line, which results in high relative errors at those time instances. By increasing the number of sections, the error reduces for all components, although C_X converges only slowly.

Absolute and relative results using the Heaviside wind profile are presented in Figs. 36 and 37. As was the case for the sigmoid wind profile, the errors for the force components that contain counteracting contributions (C_X, C_M and C_N) are highest. Similar to the results for the other wind profiles, the results converge slowest for the longitudinal force C_X.

Time histories of the forces and moments for the three velocity profiles are displayed in Figs. 38 to 41 for the hull divisions 4S3L, 3S2L, 2S2L and 1S1L, respectively.

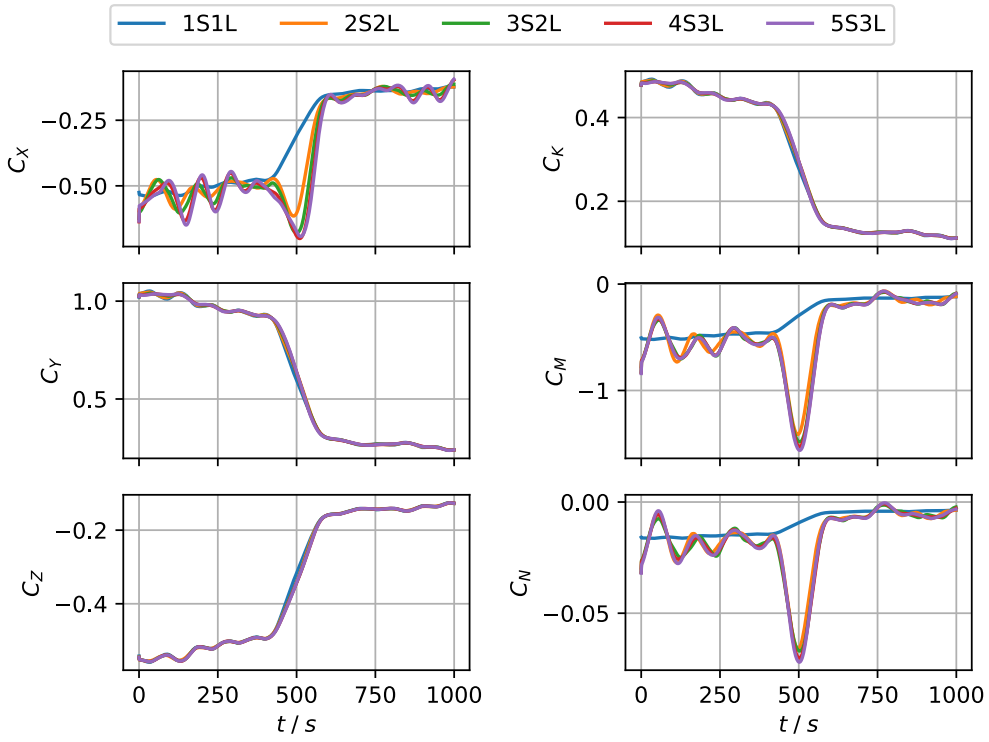

Figure 34 – Time histories of the six force components for the five hull division cases for the sigmoid wind field with random fluctuations.

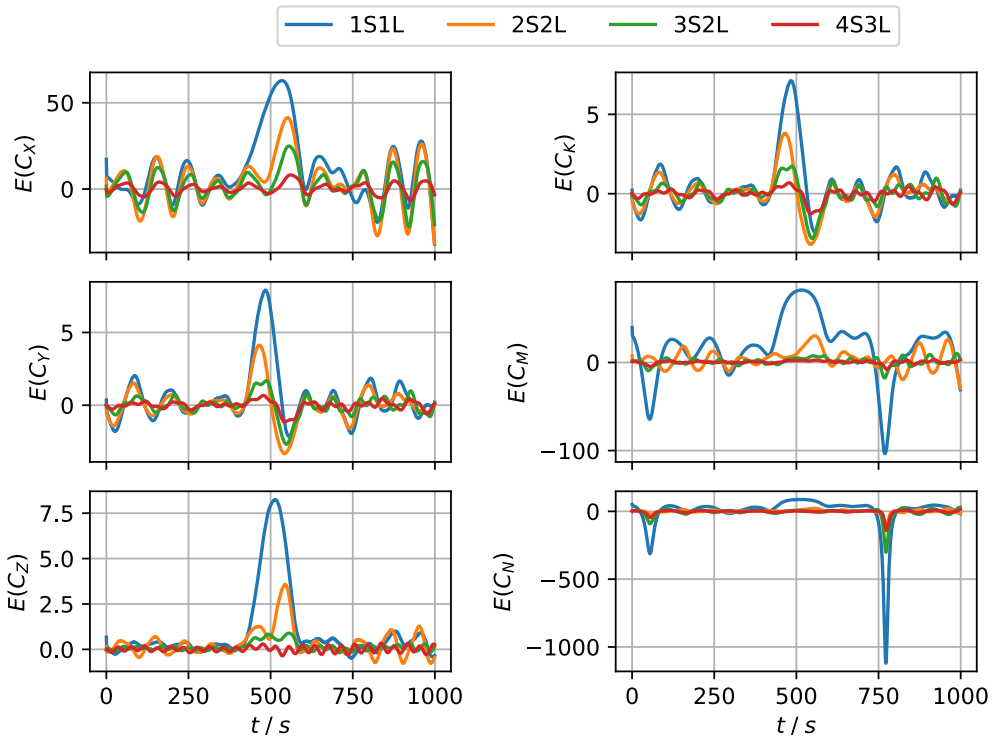

Figure 35 – Relative errors of the time histories shown in Fig. 34 using the result of 5S3L as reference.

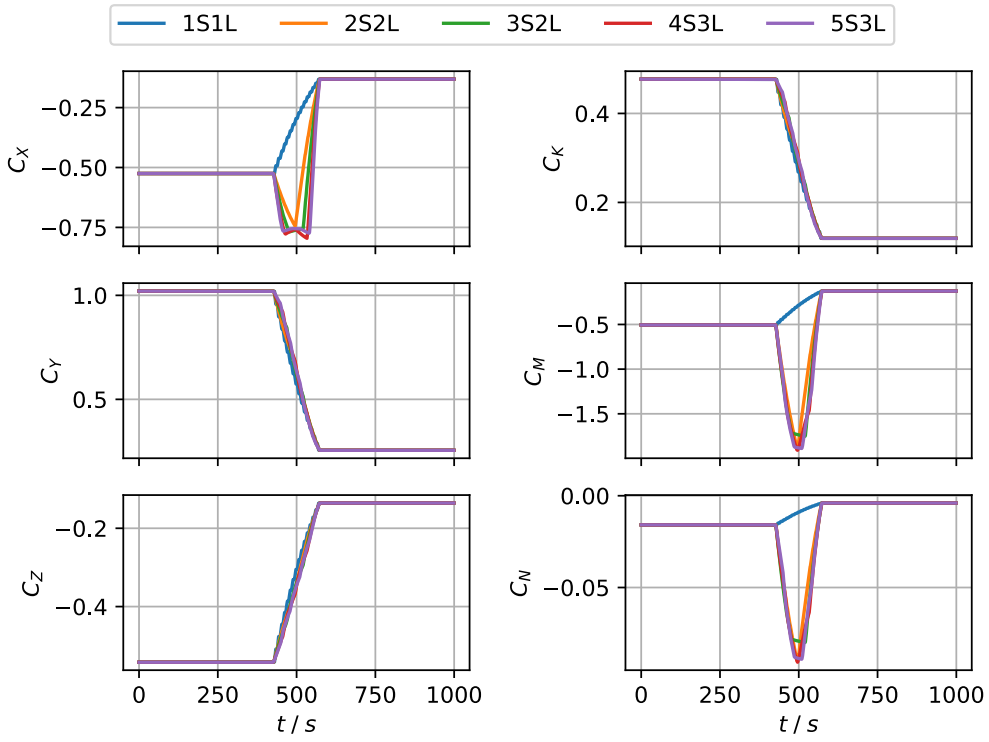

Figure 36 – Time histories of the six force components for the five hull division cases for the Heaviside wind field.

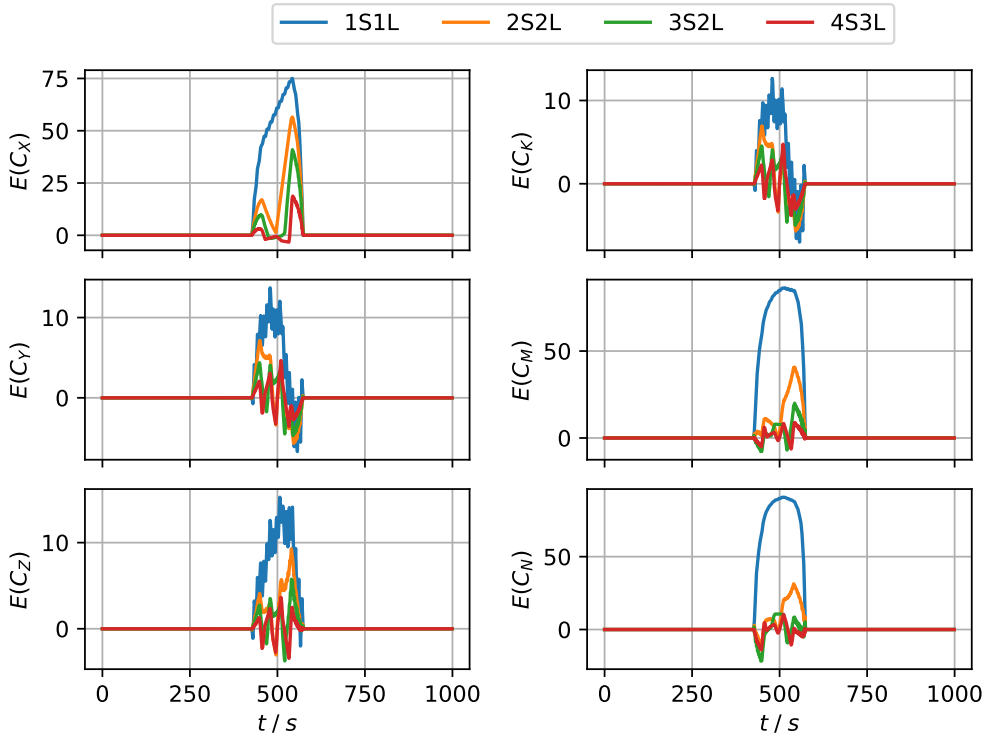

Figure 37 – Relative errors of the time histories shown in Fig. 36 using the result of 5S3L as reference.

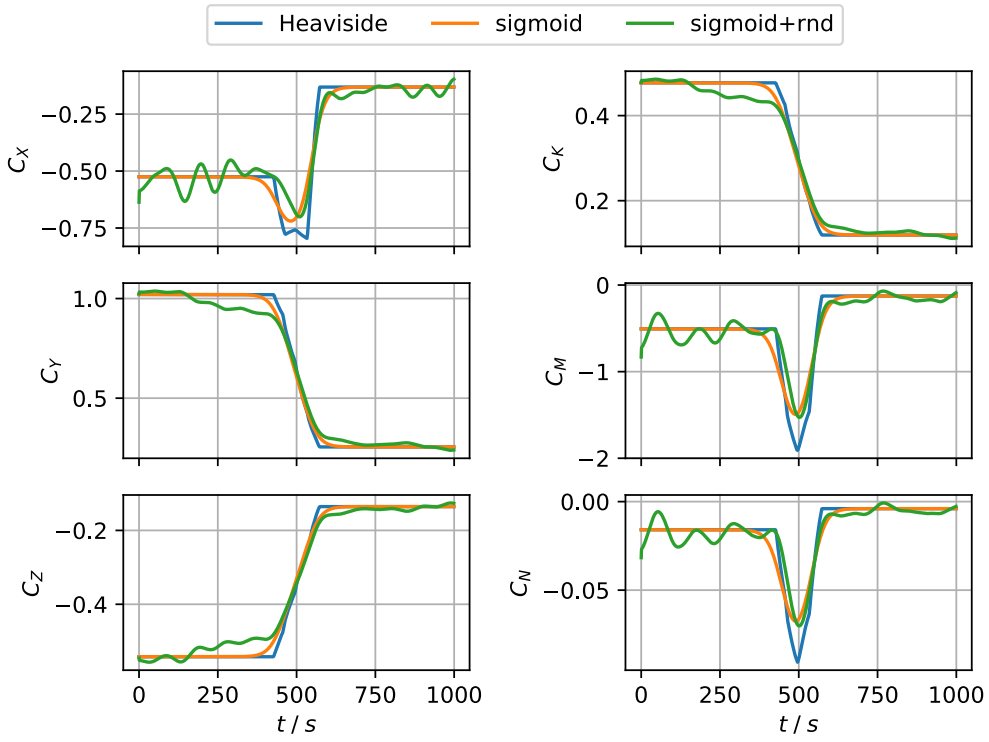

Figure 38 – Time histories of the six force components for the three velocity profiles (Fig. 5) for case 4S3L (16 point per hull section for velocity averaging).

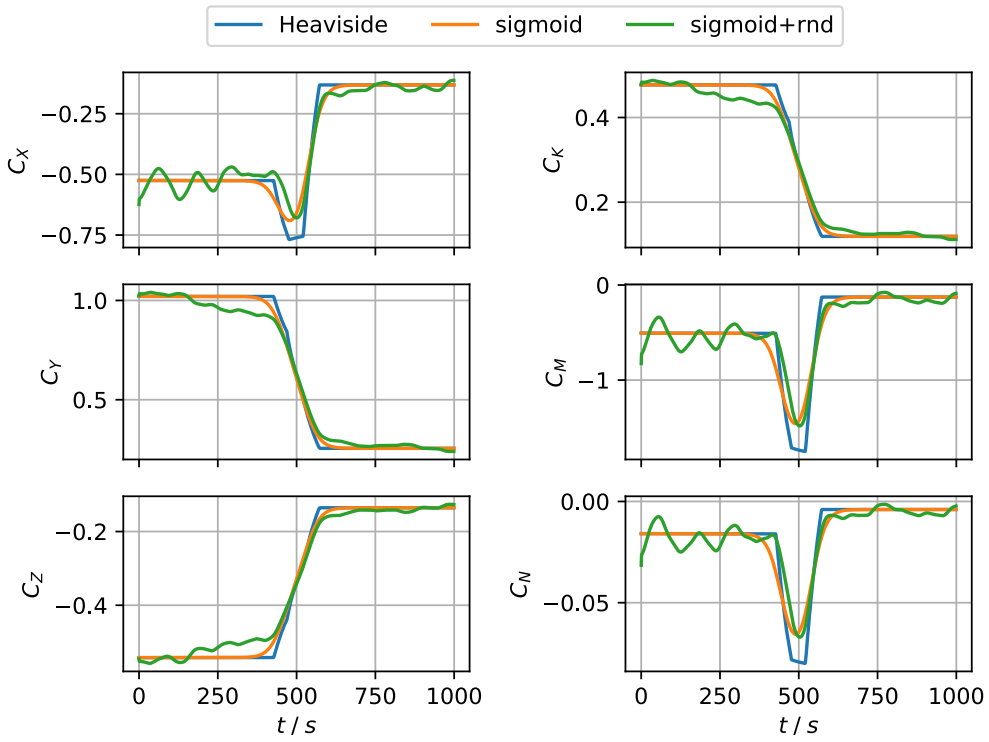

Figure 39 – Time histories of the six force components for the three velocity profiles (Fig. 5) for case 3S2L (16 point per hull section for velocity averaging).

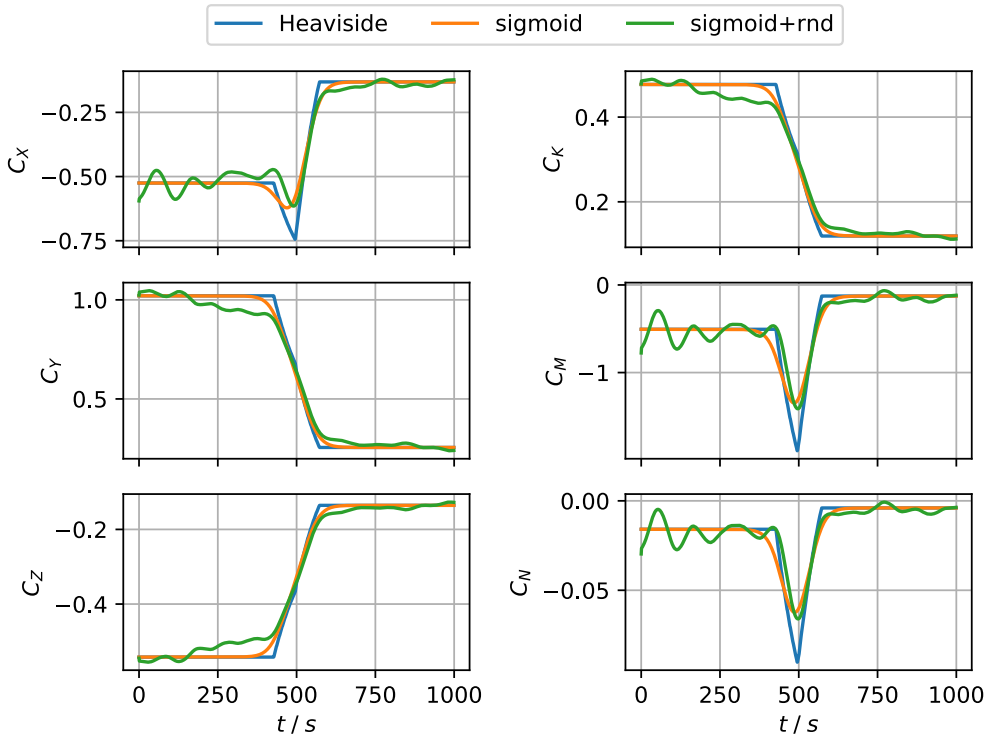

Figure 40 – Time histories of the six force components for the three velocity profiles (Fig. 5) for case 2S2L (16 point per hull section for velocity averaging).

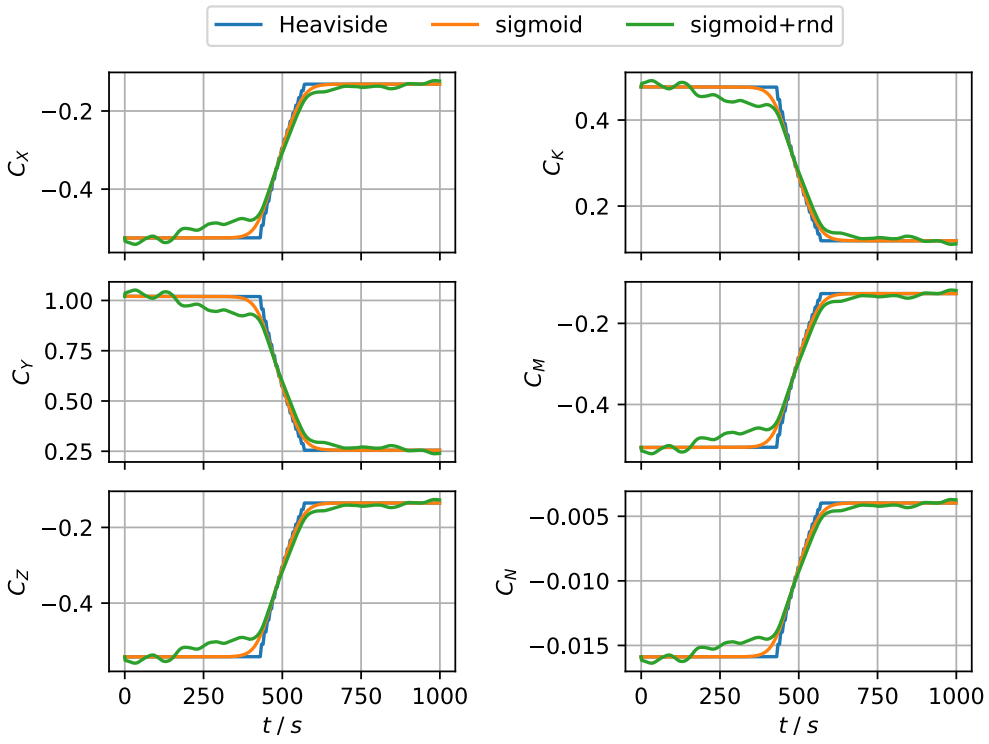

Figure 41 – Time histories of the six force components for the three velocity profiles (Fig. 5) for case 1S1L (16 point per hull section for velocity averaging).

DEPARTMENT **MOBILITY & PUBLIC WORKS**
Flanders hydraulics Research

Berchemlei 115, 2140 Antwerp
T +32 (0)3 224 60 35
F +32 (0)3 224 60 36
waterbouwkundiglabo@vlaanderen.be
www.flandershydraulicsresearch.be